

Rational discovery of small molecule inhibitor targeting invasion and tumor growth

Karthiga Santhana Kumar

University Children's Hospital Zürich

Cyrill Brunner

ETH Zurich

Matthias Schuster

University of Zurich

Levi Kopp

University Children's Hospital Zürich

Alexandre Gries

University Children's Hospital Zürich

Shen Yan

University Children's Hospital Zürich

Simon Jurt

University of Zurich

Kerstin Moehle

University of Zurich

Dominique Bruns

ETH Zurich

Michael Grotzer

University Children's Hospital Zurich

Oliver Zerbe

University of Zurich <https://orcid.org/0000-0003-0475-438X>

Gisbert Schneider

Martin Baumgartner (✉ Martin.Baumgartner@kispi.uzh.ch)

University Children's Hospital Zürich <https://orcid.org/0000-0001-9539-7204>

Article

Keywords: Drug discovery, Virtual screening, FGFR-FRS2 signaling, Medulloblastoma, Thermal Proteome profiling

Posted Date: February 15th, 2022

DOI: <https://doi.org/10.21203/rs.3.rs-1359115/v1>

License:  This work is licensed under a Creative Commons Attribution 4.0 International License.

[Read Full License](#)

Abstract

Rational targeting of proteins involved in controlling cancer cell behavior with small bioactive compounds can accelerate anti-cancer drug discovery. We report the identification of a new small molecule compound inhibitor of the FGFR adaptor protein FRS2. Pharmacophore-based computational screening combined with functional, biophysical, and structural binding analyses, led to the identification of low-molecular weight ligands that interact with the PTB domain of FRS2. By assessing the compounds' anti-invasion activity in human FGFR-driven cancer cell models, three chemically distinct bioactive molecules were shortlisted for further analysis. A lead compound was selected that specifically repressed FGFR-driven MAPK activation and matrix invasion and displayed on-target activity in cells. Proteome-wide off-target activity of the primary lead was determined and functional *in vivo* efficacy in an FGFR driven ovarian cancer model confirmed. We propose inhibition of FRS2 by a small molecular PTB domain ligand as a strategy to repress FGF signaling in FGFR-driven human cancers.

Statement Of Significance

The presented implementation of bioactive compound discovery provides a conceptual basis for targeted compound selection and accelerated drug discovery. The here identified bioactive leads targeting FGFR signaling, and cell dissemination provide a novel structural basis for further anti-cancer compound development and refinement.

Introduction

The development of anti-metastatic therapies is hampered by the lack of effective therapeutics that precisely target the proteins underlying tumor progression. The targeted disruption of protein-protein interactions (PPI) with small molecules might help to address this bottleneck. It offers an approach towards repression of specific protein functions. Virtual screening is an efficient method to explore the chemical space of the target and to select putative ligands from compound libraries^{1,2}. Small molecule PPI modulators can interact not only with protein-protein interfaces (orthosteric inhibition) but also with allosteric sites (allosteric inhibition)³. However, a main challenge in developing PPI inhibitors is to identify the disease-related and druggable PPIs.

The fibroblast growth factor receptor (FGFR) signaling pathway is a driver of both growth and dissemination of medulloblastoma (MB)⁴, the most common malignant brain tumor in childhood⁵. Invasion-promoting activities of activated FGFRs require the binding of the adaptor protein fibroblast growth factor receptor substrate 2 (FRS2) to the juxtamembrane region of FGFRs⁶⁻⁸, which couples FGFRs to downstream effectors and activates FGF signaling. The interaction of FGFRs and FRS2 thus constitutes a potentially druggable PPI with clinical relevance related to oncogenic signaling through FGFRs. Approximately 7% of all human tumors harbor an FGFR alteration⁹. FGFR1 is frequently amplified in 20-25% of squamous non-small cell lung cancer¹⁰ and 15% breast cancer¹¹, and mutated in 18% of midline gliomas¹². FGFR2 is activated by gene fusions in intrahepatic cholangiocarcinomas (15%), and in

10% of endometrial tumors^{13,14}. FGFR3 is affected by mutations in urothelial carcinomas¹⁵. Gene fusions (mainly FGFR3-TACC3) are present in glioblastomas and gliomas (3–6%^{12,16,17}), as well as in bladder cancer (2–3%¹⁸). FGFR1-4 signal via FRS2-dependent (RAS/MAPK and PI3K/AKT) and FRS2-independent (PLC- γ , JAK-STAT) pathways¹⁹. FRS2 interacts with FGFRs via its phosphotyrosine-binding (PTB) domain²⁰ and increased expression or activation for FRS2 is involved in tumorigenesis of several tumor entities^{21–25}. Targeting of FRS2 function via repressing the FRS2-directed N-myristoyltransferase repressed FGFR signaling, cell proliferation and migration in several cancer types²⁶. Selective (for example AZD4547, NVP-BGJ398 and JNJ-42756493) and non-selective (for example dovitinib or ponatinib) FGFR inhibitors have been explored for cancer therapy^{27,28}. Resistance to FGFR inhibitors can evolve similarly to other receptor tyrosine kinase (RTK) inhibitors, either by the formation of gatekeeper mutations in the catalytic domain or the activation of bypass mechanisms for downstream signaling processes through the activation of alternative RTKs²⁹ or oncogenes³⁰.

Targeting the non-enzymatically active FGFR adaptor protein FRS2 could potentially evade the evolution of FGFR gatekeeper mutations or overcome the resistance of gatekeeper FGFR-driven tumors by blocking signaling downstream of the RTK or prevent toxicities related to FGFR inhibitor treatments²⁷. An approach specifically targeting FRS2 with limited off-target activities could reduce toxicities associated with FGFR inhibitor treatments and allow for a more precisely tuned repression of FGFR signaling and additionally target FGFR-independent oncogenic functions of FRS2.

In this study, we pursued a ligand-based approach to identify small molecule ligands for the FRS2 PTB domain. We screened compounds that satisfy a pharmacophore model using computational (*in silico*) screening methodologies. We functionally tested putative hits at the molecular, cellular, and organismal levels to identify novel lead structures that bind to FRS2 and interfere with the FGFR function.

Results

Design and discovery of FRS2-PTB directed compounds

The surface of FRS2-PTB is relatively shallow and the interaction surface with the FGFR-peptide reportedly large⁸. We used LigandScout³¹ software for virtual screening of a collection of 3.5 million compounds provided by multiple suppliers (Fig. 1A). The screening was performed against pharmacophore models derived from two pockets, the first formed by the alpha-helix (A94-M105) and the beta-sheet (L33-L47), the second being complementary to the FGFR-peptide sequence I_{pep}13-R_{pep}16. The screening resulted in 14'217 hits (0.4% virtual hit rate), covering LigandScout pharmacophore scores of 52 – 76. A selection to maximize chemical diversity that excluded excessive nitro and fluorine groups was performed to result in 27 “F3 series” compounds (Fig. S1A, Table 1). We additionally virtually screened a collection of 7.68×10^4 compounds assembled from different smaller libraries (“E series”) using the pharmacophore models used for the F3 series screening. The screening resulted in a virtual hit

rate of approximately 0.2% and covered LigandScout pharmacophore-scores of 66.3 - 63.5. 31 of these compounds were selected for further downstream analysis.

Biophysical and functional validation of compounds

We first tested 27 F3 series (Fig. 1B) and 31 E series compounds (Fig. 1C) using the spheroid invasion assay (SIA)³², which measures collagen matrix invasion. We shortlisted 22 compounds of the F3 series for nano differential scanning fluorimetry (nanoDSF) analysis to test compound-FRS2-PTB domain interaction (FRS2_PTB, Fig. 1D, S2A). The addition of the FGFR peptide (FGFR_PEP, HSQMAVHKLAKSIPLRRQVTVS), which corresponds to the binding sequence of its natural ligand, had a stabilizing effect on FRS2_PTB, shifting the inflection point by $+19 \pm 0.1^\circ\text{C}$ (Fig. 1D). Using FRS2_PTB, we identified four compounds surpassing the threshold of a 2.0°C shift. One compound led to a strong negative shift of greater than -2°C (Fig. 1D). One of these four compounds showed auto-fluorescence (*) exceeding the protein's intrinsic fluorescence and was thus excluded. Compounds F3.14 and F3.18 were considered true hits. Compound F3.3 led to a modest shift of close to 1.5°C and F3.8, despite a clear positive temperature shift, displayed only moderate functional activity in the SIA (Fig. 1B). Using SIA, we thus calculated the EC_{50} of F3.3, F3.14, F3.18 and compared them to the best performing E-series compounds E12 and E25 (Fig. 1E). To increase FRS2_PTB stability and solubility, we fused the highly soluble 58 kDa protein GB1 to the N-terminus of the FRS2_PTB domain (GB1-FRS2_PTB, Fig. S2A). GB1-FRS2_PTB showed a pronounced inflection temperature at $60.2 \pm 1.4^\circ\text{C}$ (Fig. S1C). The GB1-protein alone also had a single inflection temperature at $73.6 \pm 0.8^\circ\text{C}$ (Fig. S1C). Addition of FGFR_PEP caused a shift $+10.5 \pm 0.1^\circ\text{C}$ for GB1-FRS2-PTB (Fig. S1C).

To assess the affinity of interaction of F3 series compounds and FRS2_PTB, we performed microscale thermophoresis (MST) experiments using GB1-FRS2_PTB. Binding of FGFR_PEP was assessed at 0% and 5% DMSO both in the MST trace analysis as well as in the initial fluorescence change analysis. By MST trace analysis, we estimated the affinity of FGFR_PEP to GB1-FRS2_PTB at $1.0 \pm 0.2 \mu\text{M}$. Supplemented DMSO in the buffer affected the binding of FGFR_PEP but loss of affinity was less than a factor of two. No binding was detected for F3.3 and F3.18 in the MST trace analysis. Compound F3.14 did show binding at signal:noise ratios >5 , although, overfitting of the data cannot be excluded since no upper equilibrium plateau was reached. In contrast, analysis of the fluorescence intensity change indicated clear binding of F3.14 and F3.18 to GB1-FRS2 at signal:noise ratios >5 for F3.14 and >12 for F3.18. F3.3 showed binding in only one of the duplicates. F3.14 and F3.18 displayed affinities of $12.8\text{-}19.6 \mu\text{M}$ and of $110\text{-}140 \mu\text{M}$, respectively (Fig. 1F). In conclusion, the results from the nanoDSF and MST analysis indicated that compounds F3.3, F3.14, F3.18 bind to the PTB domain of FRS2. Moreover, compounds F3.3, F3.14 and F3.18 inhibited basic fibroblast growth factor (bFGF)-induced collagen I invasion of DAOY cells to a level similar to that caused by the FGFR inhibitor Infigratinib (BGJ398)³³. A comparable inhibition of invasion was observed for compounds E12 and E25 from the E-series library (Fig. 1B,C).

Therefore, in our subsequent investigations we focused on the F3 series compounds F3.3, F3.14, F3.18 and the E series compounds E12 and E25.

Based on the results from the SIA and the biophysical assays, we concluded that compound F3.18 was a ligand of FRS2-PTB and displayed the most promising functional activity. To elucidate aspects of the structure-activity relationship, we tested 10 commercially available structural analogs of F3.18 (F18.1 – F18.10) (Fig. S1B), of which only four were soluble in aqueous solution containing 5% DMSO (F18.2, F18.7, F18.8 and F18.9). We thus tested the binding capabilities of these four compounds to GB1-FRS2_PTB in comparison to F3.18 using nanoDSF (Fig. 1G, S1D) and MST (Fig. S1E). Negative shifts of the first inflection temperature were observed for all compounds (Fig. 1G). The binding of F3.18, F18.2, F18.7, F18.8 and F18.9 was additionally tested in a nanoDSF competition assay with FGFR_PEP. GB1-FRS2_PTB was mixed with FGFR_PEP at a 1:5 ratio, and ligand competition was assayed in the presence of 500 μ M compound. A negative shift was observed in compound-mixed samples, indicating that the peptide and compounds compete for binding (Fig. S1F). We then tested the functional activity of nine F3.18 analogs using SIA (Fig. 2A). All nine compounds except F18.4 displayed invasion inhibitory activity in the SIA, with F18.7 and F18.8 performing equally well as F3.18 (Fig. 2A).

Chloride and/or strong electronegative group is necessary for optimal functional activity

F18.7 displayed the maximum inhibition of bFGF-induced cell invasion in the SIA (Fig. 2A). Both F18.7 and its parent compound F3.18 have an active NO₂ group. We designed bioisosteres of F3.18 (F3181) and F18.7 (F1871, F1872, F1873), where the NO₂ group is replaced by a carboxyl or nitrile group (Fig. S1B). All tested bioisosteres displayed a negative temperature shift in the nanoDSF assay (Fig. 1H). At 10 μ M concentration, F1871 and F1873 reduced invasion comparable to the parent compound F18.7 in the SIA assay (Fig. 2B). However, both compounds were less effective at 1 and 5 μ M concentrations compared to F18.7. Compound F3181 displayed a reduced effect compared to its parent compound F3.18 at all concentrations and compound F1872 displayed only a mild but dose-dependent reduction of bFGF-induced collagen I invasion. This variable efficacy may point to an importance of the position of the chloride group and/or of a strong electronegative group for optimal functional activity. Combining all results, we shortlisted the following hits as potential inhibitors of FRS2: F3.3, F3.14, F3.18, E12, E25, F18.2, F18.7, F18.8, F18.9, F3181, F1871, F1872, F1873 (Fig. S1B).

Next, we evaluated the selectivity of the shortlisted hits by comparing compound activity on repression of bFGF-induced cell invasion with compound activity on HGF- or EGF-induced invasion. All shortlisted compounds reduced bFGF-induced cell invasion by at least 50% (Fig. 2C). None of the compounds affected HGF-induced collagen I invasion (Fig. 2D). EGF-induced cell invasion was only moderately reduced by compounds F3.18, F18.7, F18.9 and F1873, indicating that the shortlisted hits effectively inhibit only bFGF-induced collagen I invasion. Furthermore, the invasion of the non-bFGF dependent SHH

MB tumor cell line ONS-76 remained unaffected by the treatment with the shortlisted hits (Fig. 2D), together demonstrating selective inhibition of bFGF-induced cancer cell invasion.

Confirmation and characterization of compound-target binding by NMR

To confirm binding of shortlisted hits to the PTB domain of FRS2 *in vitro*, we performed solution nuclear magnetic resonance (NMR) analysis. To fully exploit the potential of solution NMR-based screening and to allow for locating the binding sites, chemical shift assignments of the ^{15}N , ^1H correlation map are required. We used saturation transfer difference (STD) and water-ligand observed via gradient spectroscopy (WaterLOGSY) ligand observation experiments³⁴ to verify binding of the candidate molecules. We measured the rather small protein system at a reduced temperature of 7 °C and placed the saturation field in the “on-resonant” STD experiment close to the protein resonances at -0.5 ppm. Using these conditions, both, the STD and the WaterLOGSY clearly demonstrated binding of the most soluble ligands F3.14 and of the bioisostere of F18.7, F1872, to GB1-FRS2-PTB (Fig. 3A,B). The difference spectrum of the experiment displayed distinct STD signals for most of the proton resonances of F3.14 and F1872, with most prominent signals due to the aromatic positions i,j and h in F3.14 or i and j in F1872. In addition, the WaterLOGSY spectra exhibited strong positive signals at the corresponding positions, verifying the compound-protein interaction (Fig. 3A,B, S2B,C). In the case of F3.14, there were additional WaterLOGSY signals with a negative signal phase and originating from the arginine of the buffer system. These arginine resonances also interfered with the resonances a,b and c of F1872, rendering the corresponding WaterLOGSY and STD signals ambiguous.

To identify the binding site for the ligands in the FRS2-PTB domain we used chemical shift perturbation techniques derived from [^{15}N , ^1H -HSQC] spectra (Fig. S2D). We failed to reproduce refolding of FRS2 under various conditions (Fig. S2D,I) using a construct encompassing the PTB domain of FRS2 for which the structure was determined by NMR techniques⁸. Addition of the FGFR_PEP and the non-denaturing detergent CHAPS improved quality of spectra but not to the extent required (Fig. S2D,II). Even signals from the GB1-FRS2_PTB construct remained weak (Fig. S2D,III). To stabilize peptide binding, we thus covalently fused the FGFR1 peptide either to the N- or the C-terminus of the PTB through a GGS linker. The C-terminal fusion with GB1-FRS2_PTB (GB1-FRS2_PTB-FGFR_PEP, Fig. S2A) allowed to generate a good-quality [^{15}N , ^1H]-HSQC spectrum (Fig. S2D, IV). With triple-resonance NMR in combination with ^2H , ^{13}C , ^{15}N protein labeling, we could assign almost all backbone resonances from residues of the β -sheets, with the exception of the 6th β -strand (Fig. S2E). Signals from the α -helix in general were either absent or so weak that we failed to connect them to neighboring residues, possibly because the helix is not sufficiently tightly packed against the β -sheet and thus causing conformational effects.

We detected very small chemical shift perturbations (CSPs) in the GB1-FRS2_PTB-FGFR_PEP fusion after addition of the compounds, likely because the binding site is occluded by the C-terminally fused FGFR_PEP sequence. Therefore, CSPs were measured on the non-covalent GB1-FRS2_PTB:FGFR_PEP

complex, for which the affinity of the FGFR1 peptide to the protein is lower. Chemical shifts assignments of FRS2-PTB were adapted from the fusion to the complex using HNCO and HNCA spectra.

Most of the significant chemical shift perturbations were in the loop connecting β -strands 1 and 2 that covers the cleft between the two halves of the β -sandwich, and in β -strand 3 (Fig. S2E,F). In general, CSPs are larger for compound F1872, which we attributed to the better aqueous solubility of the ligand. The CSPs are located remote to the targeted binding pocket and rather spread around an area that is occluded by binding of the FGFR peptide. To investigate whether the ligands could potentially displace the peptide in this area, we removed the peptide coordinates and attempted docking of the ligands to the PTB domain, while allowing for small adjustments of the protein backbone and bigger changes for its sidechains within the putative binding pocket. Predicted docking poses that are in agreement with the CSPs are shown for F3.14 and F1873 (Fig. 3C-F). In all these poses, the aromatic rings of the ligands form π -stacking interactions with the two aromatic sidechains of Phe-87 and Phe-74. In addition, we observed several hydrogen bonds. However, since docking results in slightly different poses, the data are insufficiently precise to prove such interactions beyond any doubt. Since the FGFR peptide and the compounds share a common binding site in the PTB domain, the observed CSPs are likely rather small. Consistently, the results obtained in the ligand-observe STD and WaterLOGSY experiments using constructs without the FGFR peptide, were recorded at much lower FRS2_PTB concentrations and were much clearer.

Validation of compound activity in FGFR-driven human cancer cell lines

As we previously identified bFGF as a strong promoter of collagen I invasion in the established SHH MB cell line DAOY^{4,32}, we used this cell model for compound screening and shortlisting the hits. However, FGFR aberrations are common across human cancers and specific targeting of aberrant FGF signaling is an established strategy approved or under investigation against different types of cancer^{27,28}. To explore the applicability of the FRS2 PPI strategy as a potential treatment, we tested the efficacy of compounds in inhibiting tumor-promoting functions in various FGFR-driven cancer cell lines. We chose the following cell lines from the ATCC FGFR genetic alteration panel: DMS114 (small cell lung cancer carcinoma), HCT116 (colorectal carcinoma), SNU16 (stomach carcinoma), AGS (gastric carcinomas). In addition, based on the FGFR3 fusions and overexpression of FRS2, we also included SW780 (bladder carcinoma), RT112 (bladder carcinoma), M059K (glioblastoma) and SK-OV-3 (ovary adenocarcinoma) cell lines. We confirmed the mRNA and protein expression levels of FGFRs and FRS2 in these cell lines using qPCR (Fig. S3A,B) and immunoblotting (IB, Fig. S3C), respectively. Next, we tested bFGF sensitivities of these cell lines using SIA. SNU16 and DMS114 cells did not invade the collagen I matrix upon stimulation with bFGF. Hence, they were not further investigated using SIA. The remaining cell lines were categorized using the SIA as bFGF-sensitive (M059K, RT112, SW780) or bFGF-insensitive (SK-OV-3, AGS and HCT116), depending on whether collagen I invasion was increased by bFGF stimulation (Fig. 4A,B). We then tested the effect of the shortlisted hits on bFGF-sensitive and bFGF-insensitive cell lines in the SIA. F18.7 and its

analogs inhibited collagen I invasion in both bFGF-sensitive and bFGF-insensitive cell lines (Fig. 4A,B, S3D, S4A). In contrast, the compound E12 inhibited collagen I invasion only in bFGF-sensitive cell lines M059K, RT112 and SW780, indicating a different interference mechanism of this molecule compared to F18.7 and its analogs. F3.14 caused approximately 50% inhibition in the SK-OV-3 and AGS cells. F3.3 displayed significant repression of collagen I invasion only in SK-OV-3 and M059K cells (Fig. 4A,B, S4A). As DMS114 did not invade collagen I hydrogels, we explored basal and bFGF-induced motility of DMS114 with the Boyden transwell migration assay. We used the HCT116 cell line as control (Fig. 4C). bFGF caused only a minor increase in transwell migration of DMS114. However, treatment with F18.7 or BGJ398 caused a dose-dependent reduction of migration with a significant reduction observed at 10 μ M and 1 μ M, respectively. bFGF stimulation also caused a twofold increase in transwell migration in HCT116 cells (Fig. 4C), in contrast to the SIA, where maximal invasion occurred already in the absence of bFGF (Fig. 4A). Both basal and bFGF-increased transwell migration was abolished in HCT116 cells treated with 2.5, 5 or 10 μ M of F18.7 (Fig. 4C). The bladder carcinoma cell line RT112 expresses the FGFR3-TACC3 fusion³⁵. We found that bFGF stimulation of RT112 cells caused a significant increase in collagen I invasion. Both this increase and the basal invasion was blocked in FRS2-depleted cells (Fig. 4D), confirming that pro-migratory signaling in RT112 cells depends on FRS2. bFGF stimulation increases phosphorylation of FRS2(Y436) and this increased phosphorylation of FRS2 is reduced by two different batches of F18.7 in a dose dependent manner (Fig. 4E). Thus, F18.7 effectively blocks bFGF-induced FRS2 phosphorylation and F3.18 series compounds could also be effective for the inhibition of cancer cell invasiveness driven by FGFR3-TACC3 fusions.

We next tested the effect of the shortlisted hits on viability of the cell lines grown either in 2D (Fig. S4B) or as 3D spheroids (Fig. S4C) using the CellTiter-Glo assay. We found that compounds F18.2, F18.7, F18.8 and F1873 at a concentration between 2.7 and 20 μ M reduced viability by more than 50% in DAOY, AGS and HCT116 cells. BGJ398 reduced viability of SW780, RT112, M059K and SK-OV-3 cells in this concentration range. Next, we evaluated the effect of the shortlisted hits on the downstream effectors of bFGF signaling using immunoblotting. All compounds reduced basal or bFGF-induced phosphorylation of FRS2(pY436) in DAOY or SW780 cells, except F3.14, which was not effective in SW780 cells (Fig. 4F,G). F18.7, F1873 and BGJ398 inhibited basal or bFGF-induced phosphorylation of ERK(pT202/Y204) in DAOY, SW780, M059K, SK-OV-3, AGS and DMS114 cells (Fig. 4F-H, S4D,E,G). E12 and F3.14 also significantly reduced pERK in DAOY, SW780 and AGS cells (Fig. 4F,G, S4E,G). Compound effects on phosphorylation of AKT(pS473) were somewhat inconclusive and in E12-treated SW780 cells, we even observed an increase in pAKT (Fig. 4G). These data demonstrate functional activity of shortlisted hits in three different cellular assays across a panel of different FGFR-driven cancer cell lines, and they particularly confirmed the inhibitory efficacy of the F3.18 skeleton structure in these assays.

***In vitro* ADME-T and *in vivo* pharmacokinetic properties of E12, F3.14 and F18.7**

We next determined a range of *in vitro* pharmacokinetic properties for E12, F3.14 and F18.7 (Table 2). E12 and F3.14 are freely soluble and show a $t_{1/2}$ of clearance ($CL_{1/2}$) of 5.52 and 29 min, respectively. E12 is moderately toxic and F3.14 is not toxic in the MTT assay. F18.7 is sparingly soluble, shows a $CL_{1/2}$ of 3.62 min and is moderately toxic in the MTT assay. We nevertheless decided to test *in vivo* pharmacokinetics (PK) for these three compound classes in Balb-C mice (Fig. 5A, S5A). To determine exposure levels, we quantified compound concentrations in plasma samples at various intervals after 10 mg/kg per oral (PO, E12, F18.7) or 1 mg/kg intravenous (IV) (E12, F3.14 and F18.7) administration (Fig. 5A). E12 showed a $t_{1/2}$ of 2.71 h but only low oral bioavailability of 13 ng/ml and an area under the plasma concentration-time curve from time zero to time of last measurable concentration (AUClast) of 22 h*ng/ml. F18.7 showed oral bioavailability with a C_{max} of 1395 ng/ml, a $t_{1/2}$ of 3.83 h and an AUClast of 3333 h*ng/ml. After IV administration, C_0 of E12 was relatively low (762 ng/ml), $t_{1/2}$ was only 0.15 h and AUClast was 85 h*ng/ml. F3.14 and F18.7 displayed considerably better bioavailability (C_0 of 2703 and 2873 ng/ml, respectively), a $t_{1/2}$ of 1.55 and 1.14 and an AUClast of 413 and 398 h*ng/ml, respectively (Fig. S5A).

Evaluation of on- and off-target activity of F18.7 in cells

Significant efficacy in inhibiting FGFR-driven functions for our top hit F18.7 and relatively good bioavailability *in vivo* prompted us to explore on- and off-target activities for this compound. We used the cellular thermal shift assay (CETSA³⁶) to confirm on-target binding activity of F18.7 in DAOY cells. CETSA interrogates protein stability across a temperature gradient in intact cells. Using CETSA, we monitored FRS2 abundance in the absence and presence of 10 μ M F18.7 over a range of ten temperatures between 40.5 and 73.8°C by IB (Fig. 5B). We used beta-tubulin as negative control. We observed a negative shift in the melting curve of FRS2 in the presence of F18.7 with DT of -5.4°C (Fig. 5C). Under the same conditions, beta-tubulin displayed a weak shift with a DT_m of -1.31°C.

To explore off-target activities of F18.7, we performed thermal proteome profiling (TPP)³⁷ in intact DAOY cells. We identified approximately 8000 proteins in ~6750 protein groups at 1% false discovery rate versus Uniprot *Homo sapiens* species entries. About 6000 proteins are covered by 2 or more peptides and further analyzed. For ~5400 proteins we succeeded to fit high-quality melting curves ($R^2 > 0.8$ in both conditions) that passed the chosen filter criteria (plateau <0.3 in vehicle group). For these proteins, melting temperature (T_m) differences between DMSO and F18.7 treatments and adjusted p-values were determined (Table 3). 153 candidates showed a significant T_m difference with an adjusted p-value of <0.05, of which 91 proteins (1.64%) were stabilized and 62 (1.12%) destabilized by F18.7 treatment (Fig. 5D). The corresponding T_m differences were distributed between - 9 and + 13°C (Fig. 5 E). Altered T_m in proteins after F18.7 treatment could be direct binding or indirect downstream effects of compound-stabilized or -destabilized proteins³⁸. We therefore also explored potential direct off-target molecules of F18.7, by comparing DT_m between DMSO- or F18.7-treated DAOY cell lysates. We first confirmed on-target

activity of F18.7 on FRS2 by CETSA. As for the whole cell analysis (Fig. 5B,C), we again observed a negative shift in the melting curve of FRS2 in the presence of F18.7 with a ΔT_m of -4.83°C (ΔT_m of tubulin was -0.06°C , Fig. S5B). Independent of the treatment, the average T_m in lysates was increased by approximately 4°C compared to whole cells (Fig. S5C), which is consistent with previous reports^{38,39}. We succeeded to fit high quality melting curves for 5638 proteins. 62 proteins (1.1%) were stabilized and 68 (1.21%) destabilized by F18.7 treatment (p-value <0.05) (Fig. S5D,E, Table 4). A total of 35 (0.65%) proteins in intact cells and 24 (0.44%) proteins in the lysate displayed a T_m shift of equal or more than 5°C . We found no overlap in ΔT_m between total cells and lysates (Fig. 5E, S5E), and - probably due to low abundance - we were not able to detect endogenous FRS2 protein in neither of the two TPP approaches (Tables 3 and 4). From these experiments we concluded that F18.7 interacts with its target protein FRS2 in whole cells and lysates. However, the similar T_m shifts of approximately of 0.5% of the detected proteins reveal the interaction of F18.7 with additional proteins and indicate potential functional off-target activities of this compound.

***In vivo* maximum tolerated doses**

To establish the effective concentration for *in vivo* dose finding, we compared the EC_{50} of F18.7 in the SIA analysis (Fig. 6A) with the IC_{50} of F18.7 in cell viability assessed by 3D CellTiterGlo assay (Fig. 6B) for three bFGF-sensitive (DAOY, M059K and RT116) and three bFGF-insensitive (SK-OV-3, AGS and HCT116) cell models. For all but AGS was the EC_{50} of the SIA lower than the IC_{50} for cell viability. This indicated a selective sensitivity of most cell models tested to F18.7-mediated inhibition of cell invasiveness, and that the reduction in collagen invasion observed in F18.7-treated cells was most likely not due to toxicity.

We next set to determine the *in vivo* single-dose and multi-dose maximum tolerated dose (MTD) and *in vivo* PK of F18.7. For the single dose MTD, F18.7 was administered peroral (PO) to groups of 2 male and 2 female ICR mice. Animals received an initial dose of 30 mg/kg that was escalated up to 200 mg/kg. F18.7 was well tolerated at all the doses and only very few adverse effects such as decrease in abdominal or limb tone and yellow urine were induced. No mortality and body weight loss were observed, signifying that the tested doses (30, 100, and 200 mg/kg) were tolerated after the single bolus administration. For the multi-dose MTD, F18.7 was administered *quaque die* (qd) x5, at 200 mg/kg to groups of three female CB.17 SCID mice. F18.7 induced vocalization, hunchback and decrease in touch response, abdominal and limb tone and low limb post throughout the experimental period. No mortality was noted, but a 10% body weight loss was observed on days 1- 5 and an additional 14.6% was found from days 5 – 8.

After the MTD study, F18.7 (30, 100, 200 mg/kg, PO) was further administered to groups of two male and two female ICR mice in a PK study. Plasma and liver samples were harvested at 0.5 h after administration and the levels of F18.7 were determined by LC-MS/MS to determine exposure levels (Fig. S6B). With the 200 mg/kg administration, the desired plasma concentration of 10 $\mu\text{g}/\text{ml}$ ($> 20 \mu\text{M}$) was reached. A

second group of mice was then treated qd for 5 days and compound concentrations in plasma samples were determined at day five 0.5, 1, 2 and 6 h after compound administration (Fig. S6C). This multi-dose study showed that a plasma concentration of 7.5 mg/ml (20 μ M) was reached for at least six h after administration, and we decided to use this concentration for the *in vivo* study.

F18.7 blocks growth of ovarian cancer *in vivo*

To assess *in vivo* efficacy of F18.7, SK-OV-3 and AGS mouse xenograft models were used. Tumor cells were flank injected with 1×10^6 and 5×10^6 cells in PBS/Matrigel, respectively. BGJ398 was used as positive control compound. Animals bearing palpable tumors were randomized in groups A (vehicle control), B (F18.7) and C (BGJ398/Infigratinib), and then treated qd PO with either vehicle corresponding to group B (group A), 200 mg/kg F18.7 (group B) or 10 mg/kg BGJ398 (group C) (Fig. S6D,F). Treatment in AGS tumor-bearing mice was interrupted for 8 days at day 66 post implantation due to signs of toxicity in the F18.7-treated animals (Fig. S6F). Tumor volumes (TV) and body weight (BW) was measured before, throughout and after treatment. In the SK-OV-3 model, F18.7 treatment caused a significant reduction in tumor growth between d50 and d70 (Fig. 6C upper, S6E). Reduction was comparable to BGJ398 treatment effect, and 6/7 of the F18.7-treated mice displayed less than average control tumor growth 15d after start of treatment (Fig. 6C, lower, S6E). In the AGS model, F18.7 treatment did not significantly reduce average TV compared to control (Fig. 6D, upper). Inspection of the individual tumor growth curves revealed that TV in 4/6 of F18.7-treated animals was reduced 15d after start of treatment (d65) and plateaued between d70 and 77 compared to the average TV in control animals (Fig. 6D, lower, S6G). In 2/6 animals, no response was observed. Unexpectedly, the TV both in F18.7 and BGJ398-treated animals sharply increase after day 77, indicating re-growth of treatment-resistant tumor cells after the compound-induced lag phase. We also assessed FRS2 (Fig 6E, S7B) and ERK (Fig. S7B,C) phosphorylation as well as CD31 expression by IHC analysis in both models. Tumors of control animals displayed a heterogenous pFRS2 signal with signal enrichment in the periphery of the tumors and in central regions. The overall pFRS2 signal did neither in the tumors of the F18.7 nor in those of the BGJ398-treated animals markedly alter compared to control (Fig. 6E, S7B,C). A comparable result was obtained with pERK (Fig. S7A,B). Interestingly, however, we observed that both pFRS2 and pERK signals were reduced in regions surrounding vessels in AGS tumors of F18.7-treated animals (Fig. S7).

In conclusion, these data confirmed anti-tumor efficacy of F18.7 that is comparable to the structurally and functionally unrelated FGFR inhibitor BGJ398. We furthermore found that pFRS2 can be detected in the tumor tissue.

Discussion

The aim of this study was to identify a small molecule lead structure for disrupting FGFR-FRS2 signaling in cancer cells. We used an *in silico* discovery approach to identify putative ligands of the PTB domain of

FRS2. We confirmed direct compound-target interaction by assessing compound impact on thermal stability of the PTB domain of FRS2 and by NMR. We functionally validated anti-tumor activity in human cancer cells *in vitro* and in a tumor model of ovarian cancer *in vivo*. Using a proteome-wide compound-target identification strategy, we identified potential off-target interactions that will guide further drug development efforts.

Three chemically distinct compounds were identified that repress FGFR-dependent signaling and cancer cell invasiveness. One of these compounds, F18.7, showed anti-tumor activity in a human cancer model. F18.7 is a previously reported compound for which no specific activity was described so far. Its structural analog F18.10 has been reported as an inhibitor of several microbes and parasites and cancer targets, but not against FGFR-related proteins. Our data indicate a destabilizing effect of compound binding to FRS2, whereas binding of FGFR_PEP, a peptide corresponding to the natural ligand sequence of FGFR1, is stabilizing. This may indicate that one possible mode of action of F18.7 in cells is to compete with FGFR1-binding, to cause the destabilization of the FGFR-FRS2 complex and thereby to lead to impaired signal transmission. The predicted impaired FGFR-FRS2 interaction caused by F18.7 in cells is supported by the concomitant reduction of FRS2 Y436 phosphorylation in bFGF-stimulated cells. Furthermore, competition nanoDSF experiments showed that the destabilization effect of F18.7 was still strongly present even after co-incubation with FGFR_PEP and despite the almost 100-fold stronger affinity of the peptide, suggesting that the compound can compete with the FGFR-PTB interaction. An additional functional consequence of the destabilizing effect of F18.7 in cells and impaired FGFR signal transmission is the reduced activation of the MAPK pathway and of its downstream effector ERK. Importantly, compound effects phenocopy depletion of FRS2 by siRNA, both in collagen invasion and transwell migration as well as in ERK phosphorylation. However, the detected binding of the compounds in MST analyses with affinities of 60–140 μM is weak, as expected from small molecules in early screening hits⁴⁰.

The NMR-derived CSPs indicate that compounds F13.4, F1872 and F1873 bound to a site that is occluded by the natural FGFR ligand peptide. This site does not correspond to the pockets chosen for the virtual screening. This lack of overlap may be explained by the fact that the NMR-experiment was performed with FRS2-PTB in complex with the peptide. Indeed, the detected CSPs are small, which would be expected if the compound is competing with the peptide for FRS2 binding. Inspection of the protein:compound complexes reveals that the pocket is only partially filled. Therefore, we assume that a fragment-growth strategy could substantially improve their binding affinity in a hit-to-lead drug development effort. Nevertheless, we observed protein-compound interactions that are typically observed in drug-receptor interactions such as π -stacking or hydrogen bonds.

Our aim was to develop an alternative targeting strategy to repress FGFR-driven tumor growth and progression. FGFR alterations are not confined to one tumor entity e.g. high or low grade or adult or pediatric, which renders the assignment of FGFR alterations as tumor driving lesions more challenging⁴¹. Besides the numerous FGFR alterations in adult cancers⁹, some alterations are strongly associated with pediatric low grade neuroepithelial lesions (LGNLSs) such as FGFR1 duplication and FGFR1/3-TACC1 or

FGFR2-CTNNA3 fusions⁴¹ may be considered as hallmarks of these tumors. We found that FRS2 depletion or F18.7 treatment repressed bFGF-induced signaling in the FGFR3-TACC1 fusion-driven RT112 cells, indicating efficacy in tumors with these lesions as well. ERK is necessary for bFGF-induced invasiveness in DAOY cells⁴. However, despite the reduction of ERK phosphorylation by F18.7 in SK-OV-3 *in vitro*, we were not able to clearly correlate ERK phosphorylation with repressed tumor growth *in vivo*. Thus, FRS2 may also be involved in alternative signaling pathways to promote tumor growth. FRS2 signaling promotes tumor angiogenesis in prostate cancer⁴², and FRS2 overexpression by gene duplication is associated with tumor vascularization and poor prognosis in bladder cancer²³. Thus, the tumor growth repression in the SK-OV-3 model could also be a consequence of decreased neovascularization. Consistent with a function of FRS2 in the vasculature microenvironment is the altered FRS2Y436 phosphorylation pattern we observed in the vicinity of CD31⁺ endothelial cells in the AGS model *in vivo*. An FRS2 binding site was also discovered in the oncogenic Anaplastic Lymphoma Kinase (ALK), which is necessary for the transforming activity of ALK⁴³. ALK is overexpressed in ovarian cancer and associated with an aggressive, metastatic phenotype^{44,45}. However, the role of FRS2 binding to ALK and its potential implication in ALK-dependent tumorigenesis has not been explored yet.

MEK inhibitor trametinib induces FGFR-dependent bypass mechanisms in KRAS-mutant lung adenocarcinoma, which are blunted by depletion of FRS2⁴⁶. This suggests that FRS2 inhibition could also be suitable as a combinatorial therapy strategy in KRAS-driven tumors with acquired MEKi resistance. FGFR pathway activation also bypasses sensitivity to EGFR inhibition⁴⁷, and FGFR1 upregulation was observed in MET inhibitor resistant lung cancer⁴⁸. MET activation can cause FRS2Y436 phosphorylation in triple negative breast cancer⁴⁹, and combined inhibition of both MET and FGFR was necessary to maximally block FRS2Y436 phosphorylation and tumor initiation *in vitro* and growth *in vivo*. However, pharmacological FGFR blockade in this cancer entity caused adaptive resistance through a YAP and mTORC-dependent mechanism³⁰.

Using kinome wide thermal proteome profiling (TPP), we identified several proteins with F18.7-dependent increased or decreased thermal stability. Some of the thermal shifts observed are equal or greater to what we observed for FRS2. These proteins must be considered as potential off-targets of F18.7. However, none of the proteins with compound-altered melting temperature is a known regulator of FGFR signaling, making it unlikely that the effects of the compounds we observed on bFGF-induced signaling are the consequence of the off-target activities of the compounds.

We provide evidence for compound-mediated destabilization of the FRS2 adaptor protein as a novel mechanism to represses oncogenic FGFR signaling and invasiveness in human cancer cells and to reduce tumor growth *in vivo*. Our study thus lays a foundation for the further pre-clinical development of an FRS2 destabilizer for the treatment of human cancers with activated FGFR signaling and oncogenesis driven by the overexpression of FRS2.

Methods

Cell lines used:

DAOY human MB cells were purchased from the American Type Culture Collection (ATCC, Rockville, MD, USA). DAOY cells were cultured as described in ⁴. Cell line authentication and cross contamination testing was performed by Multiplexion by single nucleotide polymorphism (SNP) profiling. ONS-76 cells were generously provided by Michael Taylor (SickKids, Canada). RT-112 (ACC418) was purchased from the Leibniz-Institut DSMZ (Braunschweig, Germany). AGS (ATCC CRL-1739), DMS114 (ATCC CRL-2066), HCT116 (ATCC CCL-247), M059K (ATCC CRL-2365), SK-OV-3 (ATCC HTB-77), SNU-16 (ATCC® CRL5974) and SW 780 (ATCC CRL-2169) were purchased from LGC Standards GmbH, Wesel, Germany) and cultured according to LGC instructions.

-

Spheroid invasion assay (SIA) and automated cell dissemination counter (aCDc):

1000 - 2500 cells/well in 100 µl were seeded in 96 well Corning® Spheroid microplate (CLS4520, Sigma-Aldrich) or in cell-repellent 96 well microplate (650790, Greiner Bio-one). SIA and analysis was performed as described before ³². In brief: After spheroid formation (24 – 72 h after seeding), 70 µl medium was removed and replaced with the collagen mixture (2.5 mg/ml Pure Col Collagen I (Advanced Biomatrix)), DMEM 1x (from 10x stock, Sigma, D2429) and 0.4% Sodium bicarbonate (Sigma, S8761)), resulting in a final collagen concentration of 1.75 mg/ml. Embedded spheroids were stimulated with bFGF (100 ng/ml), HGF (30 ng/ml) or EGF (20 ng/ml) and distance of invaded cells quantified 24 – 48 h after embedding.

3D-Cell viability (Cell TiterGlo) assay:

Cell viability was determined using CellTiter-Glo® 2D or 3D cell viability assays (#G9242, #G9682, Promega). 500 cells/25 µl were seeded in flat bottom (#781091, Greiner bio-one) or U-low adhesion (#4516, Corning) 384-well plate, 24 h prior to treatment. Increasing concentrations of compounds are deposited on cells using a HP Digital Drug Dispenser with DMSO total volume normalization. After 48 h, the CellTiter-Glo® 2D or 3D reagent was added (volume/volume) following manufacturer's instructions. Plates were incubated at RT (room temperature) under agitation for 30 min and luminescence representing the number of viable cells was quantified with a Cytation 3 imaging reader (BioTek®). Experiments were performed independently three times with three technical replicas each.

-

Immunoblotting (IB):

Cells were serum starved o.n. and 10 µM compound or 1 µM (BGJ398) were added 3 h before stimulation with 100 ng/ml bFGF for 15 min. Cells were lysed in RIPA buffer containing protease inhibitor cocktail and lysates resolved by SDS-PAGE. Membranes were probed with primary antibodies against phospho-

FRS2, phospho-ERK1/2, ERK1/2, pAKT, AKT and tubulin. Integrated density of immuno-reactive bands was quantified using Adobe Photoshop CS3. Integrated densities of phospho bands relative to non-phospho bands of same protein were calculated and plotted as fold-change relative to untreated control conditions.

RNA expression analysis by RT-qPCR:

Cancer cells were seeded in 6-well plate for 24 h to reach 80-90% of confluency the following day. RNAs were extracted with the RNeasy® plus mini kit (#74136, Qiagen) according to manufacturer's instructions. 150 ng of RNA were used for reverse transcription in 20 µl reaction containing RNase inhibitor and using the high-capacity cDNA reverse transcription kit (#4374967, Applied Biosystems, ThermoFisher Scientific). qPCR was performed on cDNA with the TaqMan™ gene expression master mix (#4369016, ThermoFisher Scientific) using a 7900 HT fast real-time PCR system (Applied Biosystems). The relative expression level represented by the relative cDNA level was determined according to the standard curve method with a reference sample. Experiments were performed independently three times with two technical replicas.

Quantification and Statistical Analysis

Mean ± SEM are shown when means of three biological replicas are compared, mean and SD when three technical replicas are compared. Unpaired student's t-test was used to test significance of differences between two samples. For all other analyses, one-way ANOVA repeated measures test using Bonferroni's Multiple Comparison with Prism software was performed. *P*-values or adjusted *P*-values < 0.05 were considered significant (ns *p* > 0.05, * *p* ≤ 0.05, ** *p* ≤ 0.01, *** *p* ≤ 0.001, **** *p* ≤ 0.0001). Where indicated, asterisks show statistical significances between control and test sample.

Chemical libraries:

F-Series library:

Collection of commercially available fast-delivery compounds of the suppliers Asinex Corp., ChemBridge Corp., ChemDiv, Enamine, Specs, UkrOrgSyntez Ltd. And Vitas-M Laboratory Ltd.

E compound series library:

PrestwickChemicalLibrary: Collection of 1280 FDA-approved compounds.

NCCR54k: Collection of around 54k compounds intended to represent the commercially-available chemical space.

ChemicalDiversityExtension: Collection of around 14k compounds that extends NCCR54k with molecules that were initially excluded for various reasons (e.g. molecular weight, number of stereo-centers)

PPI: Collection of around 5k compounds targeted at disrupting protein-protein interactions.

NaturalProducts: Collection of around 2.5k commercially available natural compounds. These compounds are enantiomerically pure but their stereo chemistry is not always known. Therefore, several of them appear to have identical structure (because of the unspecified stereocenters) but the suppliers guarantee that different catalog IDs correspond to different compounds.

-

In silico screening methods:

Relevant PPIs were analyzed by iPRED analysis based on the only known structure of the FRS2-PTB 1XR0. Calculations were performed via the online available iPRED-tool. Virtual screening was performed with LigandScout based on PDB 1XR0. The co-crystallized peptide was removed, the surface analyzed for pockets by the in-built pocket calculator. Two shallow pockets the first formed by the alpha-helix (A94-M105) and the beta-sheet (L33-L47), the second being complementary to the FGFR-peptide sequence I_{pep}13-R_{pep}16 (FGFR_PEP: HSQMAVHKLAKSIPLRRQVTVS), were identified and isolated. Amino acids were charged at pH 7 according to their pK_A and energy minimized. Apo Site grids were calculated with a maximum of 4 H-bond acceptors, 3 H-bond donors, 2 positively ionizable groups, 1 negatively ionizable group, 2 aromatic groups and 4 hydrophobic moieties. Accessibility was considered in the calculation. The generated pharmacophore was run against a database containing all fast-delivery compounds of the suppliers Asinex Corp., ChemBridge Corp., ChemDiv, Enamine, Specs, UkrOrgSyntez Ltd. And Vitas-M Laboratory Ltd. with an overall compound number of 3.5 million (F-series) and against a collection of compounds from libraries listed above (E-series). Screening was performed under the Pharmacophore Fit-model with maximally 4 pharmacophoric features being omissible in order to be considered. Hits from both pockets were then combined, ranked by the provided score and selected based upon chemical diversity. Fragment-based screening and docking was performed with LigandScout vers. 4.2.1 (Inte:Ligand, Vienna, Austria) and data analyzed with Microsoft Office Excel 365 (Microsoft Corp., Seattle, USA).

-

Nano-Differential Scanning Fluorimetry (nanoDSF):

Assay establishment and pilot nanoDSF experiments were performed with a Tycho® system. Each experiment was performed by mixing the protein and ligand of interest at a 1:1 ratio and subsequent incubation for 15-30 min at room temperature. Controls of protein alone and ligand alone in identical

buffer compositions as for the complex were measured accordingly. The temperature gradient ranged from 35 to 95°C, and the heating rate was 30°C/min. Inflection temperatures T_I were calculated from the first derivative of the spectra obtained at the ratio of the signals at 350 nm to those at 330 nm. ΔT_I of a complex was calculated as following: $\Delta T_{I,complex} = T_{I,complex} - T_{I,protein}$

The in-built software version 1.1.5.668 (NanoTemper Technologies, Munich, Germany) and Microsoft Office Excel 365 (Microsoft Corp., Seattle, USA) was used for data analysis. Data was plotted with GraphPad Prism vers. 8.3.0 (GraphPad Software, San Diego, USA).

Purified FRS2_PTB or GB1_FRS2_PTB protein tagged with 6x Histidine residues and Guanine nucleotide-binding protein subunit beta (GB1) were diluted in the protein buffer (100 mM sodium phosphate, 50 mM NaCl, 0.5 mM EDTA, 50 mM arginine, 1 mM TCEP, pH 7.0) to 30 μ M, GB-1 to 40 μ M. FGFR_PEP, compounds or paracetamol (PARA) as negative control were dissolved at 1 mM in the protein buffer supplemented with 10% DMSO. Compound and protein were mixed at 1:1 volume ratio yielding a final concentration of 15 μ M and 20 μ M for FRS2_PTB/GB1_FRS2_PTB and GB1, respectively, as well as 500 μ M for FGFR_PEP or compounds. The mixture was incubated for 15 min. Each compound was measured in triplicates. Protein controls were measured in six replicates in the beginning. The quality of the screen was assessed by the Z-factor. nanoDSF validation studies were performed on a Prometheus® system in high sensitivity capillaries. Samples were heated with 1°C/min from 20 to 95°C. Each compound was measured in triplicates. GB1-FRS2_PTB and GB1 were diluted in the protein buffer (100 mM sodium phosphate, 50 mM NaCl, 0.5 mM EDTA, 50 mM arginine, 1 mM TCEP, pH 7.0) to 30 μ M. Compounds F3.3, F3.4, F3.18 as well as the F3.18 analogues were dissolved in 100% DMSO at 50 or 100 mM and further diluted to 1 mM with a final DMSO-concentration of 100%. FGFR_PEP was dissolved at 1 mM in the protein buffer supplemented with 10% DMSO. Compound and protein were mixed at 1:1 volume ratio yielding final concentrations of 15 μ M protein and 500 μ M for the compounds. FGFR_PEP was measured against both GB1-FRS2_PTB and GB1, all other compounds only against GB1-FRS2_PTB. The mixture was incubated for 15 min before measurement. The data was analyzed for both the ratio of signals at 330 and 350 nm and at 350 nm alone.

Microscale thermophoresis (MST):

Protein labeling for MST was performed with the 2nd Generation BLUE-NHS dye. GB1-FRS2_PTB- was labelled at 20 μ M with 60 μ M dye and incubation for 30 min in the dark at room temperature. The labelling was performed in the protein buffer without arginine supplementation. It was rebuffed to protein buffer (100 mM sodium phosphate, 50 mM NaCl, 0.5 mM EDTA, 50 mM arginine, 1 mM TCEP, pH 7.0). The dye was subsequently removed by gravitational flow chromatography and the protein concentration determined by UV-spectroscopy.

The assay was established with the FGFR_PEP. The peptide was dissolved in protein buffer with and without 10% DMSO supplementation in a 1:1 serial dilution from 1 mM to 61.04 nM. A total volume of 10

μl of 50 nM labelled protein was added to 10 μl of the peptide dilution series for a final labelled protein concentration of 25 nM. The samples were incubated for 15 min at RT. Premium-coated capillaries were used, excitation power was set at 20%, MST-power to 40% (4 K temperature gradient) with a laser-on time of 20 s and a laser-off time of 3 s. Temperature was set to 25°C. Each measurement was repeated twice. The interaction was measured in duplicates for the non-DMSO-supplemented buffer and in triplicates for DMSO-supplemented buffer. The compounds F3.3, F3.14, F3.18 as well as the analogs 18.2, 18.7, 18.8 and 18.9 were dissolved in 100% at 50 or 100 mM and further diluted to 1 mM with a final DMSO-concentration of 100%. The compounds were diluted in a 1:1 serial dilution from 1 mM to 61.04 nM in protein buffer supplemented with 10% DMSO. 10 μl of 50 nM labeled protein was added to 10 μl of each compound dilution for a final labeled protein concentration of 25 nM and a DMSO-concentration of 5%. The samples were incubated for 15 min, and MST assessed as described above. Each measurement was repeated twice. The interaction was measured in two independent duplicates. LIFC was observed in all measurements. Subsequently, 10 μl of compounds F3.3, F3.14 and F3.18 at 2 mM, 1 mM, 500 and 250 μM were incubated with 10 μl of 50 nM dye to yield final compound concentrations from 1 mM to 125 μM in a 1:1 dilution series and 25 nM dye concentration. The mixture was then measured for their initial fluorescence once.

MST-experiments were performed with MO.Control vers. 1.6 (NanoTemper Technologies, Munich, Germany) and data analyzed with MO.Analysis vers. 2.3 (NanoTemper Technologies, Munich, Germany). Data was plotted with GraphPad Prism vers. 8.3.0 (GraphPad Software, San Diego, USA).

Expression and Purification:

The PTB domain of human FRS2, residues 15 to 135, were cloned into a pEM3BT2 vector as a fusion with an N-terminal 6x histidine tag, GB1 with or without FGFR1 peptide (FGFR_PEP HSQMAVHKLAKSIPLRRQVTVS) and was then used to transform BL21 (DE3) cells for plasmid DNA amplification and protein expression. To induce protein expression, the transformed clones were cultured at 37°C in labelled M9 media supplemented with 100 $\mu\text{g}/\text{ml}$ of ampicillin using $^{15}\text{N}\text{-NH}_4\text{Cl}$ and ^{13}C -glucose as the sole sources of ^{15}N and ^{13}C . When the culture reached an OD_{600} of 0.6 to 0.8, protein expression was induced by adding 1 mM of IPTG at 25°C overnight.

The bacterial cells were collected by centrifugation at 5000 x g for 15 min and the pellets lysed by adding 10 mg/ml of lysozyme and sonication. The lysates were then centrifuged for 30 min at 18,000 rpm at 4°C. The supernatants were filtered using a 0.2 μm membrane and passed on an equilibrated, 5 ml Ni-NTA column using ÄKTA prime at 4°C. The protein/resin complex was then washed with 5 column volumes each using low salt wash buffer and high salt wash buffer. The protein was eluted from the resin using the elution buffer containing 100 mM Tris, 50 mM NaCl and 500 mM (pH 7.0) imidazole. Following SDS-PAGE analysis of the eluted fractions, the protein was dialyzed overnight against the buffer containing 50 mM phosphate buffer, 50 mM NaCl, 1 mM TCEP and 0.5 mM EDTA, pH 7.0 at 4°C.

The protein fractions were then pooled and concentrated to 250 μM using Amicon Ultra – 4 (10 KDa cutoff) centrifugal filters. The final protein concentration was determined by measuring absorbance at 280 nm using a nanodrop instrument and further used for NMR analysis.

-

NMR spectroscopy:

NMR experiments were recorded using 250 μM solutions of proteins in 50 mM phosphate buffer, 50 mM NaCl, 1 mM TCEP and 0.5 mM EDTA, pH 7.0. All NMR experiments were recorded at 310 K on Bruker Avance-Neo 600 or 700 MHz spectrometers equipped with cryoprobes. For backbone assignment of the GB1-FRS2_PTB_FGFR_PEP fusion protein a ([79% ^2H , 99% [^{13}C , ^{15}N])-labeled sample was used.

Experiments were selected from the Bruker standard pulse sequence library. [^{15}N , ^1H]-HSQC experiments were of the sensitivity-enhance type⁵⁰ and comprised spectral widths of 14(F2, ^1H) and 36 (F1, ^{15}N) ppm with 1024*128 complex data points. HNCACB / HN(CO)CACB spectra were used to link sequential amide groups via $\text{C}\alpha/\text{C}\beta$ resonances. In addition, sequential connection was confirmed via common carbonyl resonances using the HNC(O) and HN(CA)CO experiments. The usage of the HN(CACO)NH experiment proved to be particularly useful by establishing sequential contacts in cases where the $\text{C}\alpha/\text{C}\beta$ correlations were missing by directly establishing sequential ^{15}N connectivity. All spectra were processed in TOPSPIN using linear prediction and spectra were analyzed in the program CARRA.

STD and WaterLOGSY experiments were measured at 7°C on a Bruker AvNEO 600 spectrometer equipped with a TCI cryoprobe. In the STD experiments saturation was achieved by applying a series of Gaussian-shaped pulses at a RF field strength of 54 Hz (max.) for 3 s at -0.5 ppm (-40 ppm for the reference experiment) and 512 scans were accumulated. The WaterLOGSY was measured with 256 scans and a mixing time of 1.5 s. A 7.5 ms Gaussian-shaped 180° pulse was used to control the water magnetization. For both experiments samples of 25 μM GB1-FRS2_PTB with a 20-fold excess of ligand (500 μM) were used or with the ligand alone for the control experiment.

-

Thermal Protein Profiling (TPP) in intact cells:

Two 15 cm dishes with 0.5×10^6 DAOY cells per dish were grown in full medium o.n. Prior to compound treatment, cells were washed once in PBS. Complete growth medium containing 10 μM compound was then added and cells incubated for another 90 min at regular culture conditions. Medium was removed, cells washed with PBS containing 10 μM compound and detached using trypsin containing 10 μM compound. Trypsin was neutralized using regular growth medium containing 10 μM compound and cells were collected by centrifugation (300 x g, 25°C, 5 min). After one more wash in PBS containing 10 μM compound, cell pellet was resuspended in 220 μl PBS containing 10 μM compound. Ten 20 μl aliquots were dispensed in a pre-cooled PCR plate, which was sealed with aluminum foil and placed on ice until heat treatments. Heat treatment was performed in a gradient PCR machine. The following temperatures

were used: 40.5, 43.6, 46.2, 48.8, 51.2, 53.8, 56.4, 58.3, 61.7 and 73.8°C for three min. Plate with samples was kept at RT for 3 min and then kept on ice until centrifugation for 2 min at 500 g at RT.

Cells were lysed by adding 30 µl TPP lysis buffer (PBS, 1.33% IGEPAL, 1.66 mM MgCl₂, 1.66 µg/ml cOmplete protease Inhibitors, 1.66 µg/ml PhosStop, 416.6 U/ml benzonase) per sample, resulting in a final concentration of 0.8% IPEGAL, 1 mM MgCl₂, 1 µg/ml cOmplete protease Inhibitors, 1 µg/ml PhosStop, 250 U/ml benzonase. Samples were incubated 1h at 4°C, with shaking at 500 rpm. Samples are filtered using a MultiScreenHTS HV-Filterplate (Merck, MSHVN4510). Membrane wells were prewetted with 50 µl PBS and centrifuged at 2000 x g, RT, 3 min. The lysates were centrifuged at 2000 g, RT, 3 min and 40 µl of each supernatant was transferred to the filter plate and centrifuged at 500 g at RT for 5 min. Flow-through of samples was collected in a fresh 96-well plate and kept on ice. 20 µl of samples was snap-frozen and stored at -80°C for further analysis by mass-spectrometry. 5 µl was used for protein concentration determination using BCA assay.

Thermal Protein Profiling (TPP) in lysates:

Four 15 cm dishes with 0.5 × 10⁶ DAOY cells per dish were grown in full medium o.n. Medium was then removed, cells washed with PBS, detached using trypsin, collected in regular growth medium, centrifuged (300 g, 25°C, 5 min), washed with PBS and resuspended in 550 µl ice-cold PBS. Cells were lysed with three freeze-thaw cycles (freeze in liquid N₂, thaw in 25°C heat block, vortex quickly) and lysates were placed in aliquots of 250 µl on ice. Compound or solvent was added to 10 µM final concentration and samples were incubated 20 min at 4°C under rotation. Ten 20 µl aliquots were dispensed in a pre-cooled PCR plate, which was sealed with aluminum foil and placed on ice until heat treatments. Heat treatment was performed in a gradient PCR machine with the following temperatures 40.5, 43.6, 46.2, 48.8, 51.2, 53.8, 56.4, 58.3, 61.7 and 73.8°C for three min. Plate with samples was kept at RT for 3 min and then kept on ice until centrifugation for 2 min at 500 x g at RT.

The soluble fraction of the lysates was recovered by addition of 30 µl TPP lysis buffer (PBS, 1.33% IGEPAL, 1.66 mM MgCl₂, 1.66 µg/ml cOmplete protease Inhibitors, 1.66 µg/ml PhosStop, 416.6 U/ml benzonase) per sample, resulting in a final concentration of 0.8% IPEGAL, 1 mM MgCl₂, 1 µg/ml cOmplete protease Inhibitors, 1 µg/ml PhosStop, 250 U/ml benzonase. Samples were incubated 1h at 4°C, with shaking at 500 rpm. Samples are filtered using a MultiScreenHTS HV-Filterplate (Merck, MSHVN4510). Membrane wells were prewetted with 50 µl PBS and centrifuged at 2000 g, RT, 3 min. The lysates were centrifuged at 2000 g, RT, 3 min and 40 µl of each supernatant was transferred to the filterplate and centrifuged at 500 g at RT for 5 min. Flow-through of samples was collected in a fresh 96-well plate and kept on ice. 20 µl of samples was snap-frozen and stored at -80°C for further analysis by mass-spectrometry. 5 µl was used for protein concentration determination using BCA assay.

Cellular thermal shift assay (CETSA) using IB:

For a cellular thermal shift assay (CETSA) run, 7.5 µl of the flowthrough samples of the TPP preparation was mixed with 3 µl 4x Laemmli buffer containing 50 mM DTT and boiled for 5 min at 95°C. 10 µl of each sample was assayed by immunoblot using antibodies against FRS2 and beta-tubulin.

-

Mass spectrometry – ESI MS:

Sample preparation: Protein samples were processed using a modified SP3 clean-up and digestion procedure on a KingFisher Flex (Thermo). In short, protein samples were reduced/alkylated using 2 mM TCEP, 15.6 mM CAA for 30 min at 60°C. Subsequently, samples were adjusted to 50% Ethanol and bound to 100 µg magnetic beads. Bound proteins were washed three times with 80% ethanol and on-bead digested overnight in 50 mM TEAB including Trypsin/Lys-C (1:50, enzyme:protein) at 37°C. Resulting peptides were recovered and dried to completeness.

For isobaric labelling, peptides were resuspended in 20 µl 50 mM TEAB and 0.1 mg TMT reagent was added in 5 µl anhydrous ACN and incubate for 1h at room temperature with shaking. Unused labelling reagent was quenched by adding 1.25 µl of 5% hydroxylamine solution and incubation for 15 min at RT. Quenched samples were pooled and cleaned using C18 solid phase extraction and subsequently dried down.

High pH reversed-phase (RP) peptide fractionation: Peptides were dissolved in 100 µl of 9 mM ammonium formate, and 90 µl were loaded onto a XBridge Peptide BEH C18 column (Waters, 130 Å, 3.5 µm, 1 mm x 100 mm) on an Agilent 1200 HPLC. The samples were separated into 64 fractions using a gradient of 2% ACN, 9 mM ammonium formate (pH 10) to 40% ACN, 9 mM ammonium formate (pH 10) in 60 min at a flow rate of 1 ml/min and concatenated into 8 fractions before drying the peptides to completeness.

LC-MS Data Acquisition: LC-MS analysis of pooled high-pH RP fractions was conducted on a Q Exactive HF (Thermo Fisher Scientific) mass spectrometer operated in-line with an ACQUITY UPLC M-Class (Waters). A 75 µm forward-trap elute configuration was used for peptide separation on a 25 cm x 75 µm, 1.8 µm HSS T3 analytical column (Waters). The separating linear gradient covered 5% ACN, 0.1% FA to 35% ACN, 0.1% FA in 90 min at a flow rate of 400 nl/min. Mass spectra were essentially recorded in data dependent mode (top25). MS2 spectra were acquired by isolating peptide precursor ions at 0.7 Da, followed by HCD fragmentation at an NCE of 33 (AGC target: 1e5, maxIT: 87 ms, R: 45000). Dynamic exclusion was set to 30 s and charge states of the type unassigned, 1, ≥ 6 was ignored.

Data analysis: Peptide and protein identification, as well as protein-level quantification relative to the lowest temperature (TMT channel 126), was conducted using Proteome Discoverer 2.5.0.4. Melting curve fitting was conducted using the Bioconductor TPP package 3.13.

In vitro absorption, distribution, metabolism, and excretion – toxicity (ADMET) assays:

In vitro ADME-T assays were performed by Cyprotex (Cyprotex Discovery, Cheshire, UK). *Semi-Thermodynamic solubility*: The shortlisted hits were added to a 96-well plate in quadruplicate and 1 x PBS was added to give a maximum concentration of 100 µM. The solution was agitated at ambient temperature overnight. The solutions were then centrifuged for 30 min at 3000 rpm at RT. The supernatant was removed and centrifuged for a further 30 min under the same conditions. An aliquot of the resulting supernatant was diluted in 50% methanol in water (containing an internal standard for MS analysis) prior to analysis by LC-MS/MS. A standard curve was produced by diluting the 10 mM DMSO stock with DMSO to give concentrations of 1 mM and 0.1 mM. These stocks were diluted in 50% methanol in water (containing an internal standard for MS analysis) prior to analysis by LC-MS/MS. The solubility of the shortlisted hits was calculated from a linear or quadratic fit of the standard curve.

Microsomal metabolic stability: Pooled liver microsomes were purchased from Xenotech (H0500) and were stored according to manufacturer's instructions prior to use. Microsomes (final protein concentration 0.5 mg/ml), 0.1 M phosphate buffer pH 7.4 and shortlisted hits (final substrate concentration 1 µM; final DMSO concentration 0.25%) were pre-incubated at 37°C prior to addition of NADPH (final concentration 1 mM) to initiate the reaction. A minus co-factor control incubation was included for each compound tested where 0.1 M phosphate buffer pH 7.4 was added instead of NADPH. Two control compounds were included with each species. All incubations were performed singularly for each shortlisted hit. Each compound was incubated for 0, 5, 15, 30 and 45 min. The minus co-factor was incubated for 45 min only. The reactions were stopped by transferring incubate into acetonitrile at the appropriate time points in a 1:3 ratio. The termination plates were centrifuged at 3000 rpm for 20 min at 4°C to precipitate the protein. Following protein precipitation, the supernatant were combined in cassette of up to 4 compounds, internal standard for MS analysis was added and samples were analyzed using LC-MS/MS. From a plot of ln peak area ratio (compound peak area/internal standard peak area) against time, the gradient of the lines were determined. Subsequently, half-life and intrinsic clearance were calculated using the following equations.

Elimination rate constant (k) = (- gradient)

Half-life ($t_{1/2}$) (min) = 0.693/k

Intrinsic clearance (CL_{int}) (µl/min/mg protein) = $V \times 0.693 / t_{1/2}$

Where V = Incubation volume (µl) / Microsomal protein (mg)

CaCo-2 permeability (Bi-directional): Caco-2 cells obtained from the ATCC were used between passage numbers 40 - 60. Cells were seeded onto Millipore Multiscreen Transwell plates at 1×10^5 cells/cm². The cells were cultured in DMEM and media was changed every two or three days. On day 20, the permeability

study was performed. Cell culture and assay incubations were carried out at 37°C in an atmosphere of 5% CO₂ with a relative humidity of 95 %. On the day of the assay, the monolayers were prepared by rinsing both apical and basolateral surfaces twice with Hanks Balanced Salt Solution (HBSS) at the desired pH warmed to 37°C. Cells were then incubated with HBSS at the desired pH in both apical and basolateral compartments for 40 min to stabilize physiological parameters.

The dosing solutions were prepared by diluting the test compound with assay buffer to give a final compound concentration of 10 µM (final DMSO concentration of 1% v/v). The fluorescent integrity marker lucifer yellow was also included in the dosing solution. Analytical standards were prepared from test compound DMSO dilutions and transferred to buffer, maintaining a 1% v/v DMSO concentration.

For assessment of A-B permeability, HBSS was removed from the apical compartment and replaced with test compound dosing solution. The apical compartment insert was then placed into a companion plate containing fresh buffer (containing 1% v/v DMSO). For assessment of B-A permeability, HBSS was removed from the companion plate and replaced with test compound dosing solution. Fresh buffer (containing 1% v/v DMSO) was added to the apical compartment insert, which was then placed into the companion plate.

At 120 min, the apical compartment inserts and the companion plates were separated, and apical and basolateral samples were diluted for analysis.

Compound permeability was assessed in duplicate. Compounds of known permeability characteristics were run as controls on each assay plate.

Test and control compounds were quantified by LC-MS/MS cassette analysis using a 7-point calibration with appropriate dilution of the samples. The starting concentration (C₀) was determined from the dosing solution and the experimental recovery calculated from C₀ and both apical and basolateral compartment concentrations. The integrity of the monolayer throughout the experiment was checked by monitoring lucifer yellow permeation using fluorimetric analysis.

The permeability coefficient (P_{app}) for each compound was calculated from the following equation:

$$P_{app} = (dQ/dtC_0 \times A)$$

where dQ/dt was the rate of permeation of the drug across the cells, C₀ was the donor compartment concentration at time zero and A was the area of the cell monolayer. C₀ was obtained from analysis of the dosing solution.

Efflux ratio (ER) was calculated from mean A-B and B-A data. This was derived from:

$$ER = P_{app}(B-A) / P_{app}(A-B)$$

Three control compounds were screened alongside the test compounds, atenolol (human absorption 50 %), propranolol (human absorption 90 %) and talinolol (a substrate for P-glycoprotein).

Cell Viability (Cytotoxicity testing using HepG2): HepG2 human hepatocellular carcinoma cells were plated on 96-well tissue culture polystyrene plates for 24 h prior to dosing of the cells. The shortlisted hits were diluted in DMSO and serial dilutions are made 1% DMSO in growth media. Compounds at 8 concentrations in triplicate was then incubated for 72 h. Appropriate blanks and controls were run alongside the assay. One h prior to the end of the incubation period, the cells were loaded with MTT [yellow; 3-(4,5-dimethyl-2-thiazolyl)-2,5-diphenyl-2H-tetrazolium bromide], the plates were dried and re-solubilized using DMSO. The plates were then scanned at 570 nm using a plate reader.

The minimum effective concentration was determined from the lowest concentration whose mean value exceeds the significance level, provided either a clear dose-response relationship was observed, or at least two consecutive concentration points were above the significance level.

-

In vivo bioavailability analysis with E12, F3.14 and F18.7:

In vivo bioavailability studies were performed by Pharmacology Discovery Services Taiwan, Ltd., (New Taipei City, Taiwan). Male ICR mice weighing 20 - 30 g were provided by BioLasco Taiwan (under Charles River Laboratories Licensee). Animals were acclimated for 3 days prior to use and were confirmed with good health. All animals were maintained in a hygienic environment with controlled temperature (20 - 24°C), humidity (30% - 70%) and 12 hours light/dark cycles. Free access to sterilized standard lab diet [MFG (Oriental Yeast Co., Ltd., Japan)] and autoclaved tap water. A pharmacokinetic (PK) study was performed in male ICR mice following intravenous (IV) and oral (PO) administration of compound F18.7 and E12 and IV administration of the test compound F3.14. The three test compounds (F18.7, E12 and F3.14) were formulated in 1% dimethyl sulfoxide (DMSO)/10% Solutol® HS-15/ phosphate buffered saline (PBS) at 0.2 mg/mL and 1 mg/mL for IV and PO administration, respectively. The dosing volumes were 5 ml/kg for IV and 10 ml/kg for PO. The dose was 1 mg/kg for IV and 10 mg/kg for PO routes. The plasma samples were collected and at 3, 10, 30, 60, 120, 240, 480, and 1440 min after IV and 10, 30, 60, 120, 240, 360, 480, and 1440 min after PO administration. $T_{1/2}$ was calculated as follows:

$$t_{\frac{1}{2}} = \frac{\ln_2 \cdot V_D}{CL}$$

In vivo single dose and multi dose MTD studies with F18.7:

In vivo MTD studies were performed by Pharmacology Discovery Services Taiwan (New Taipei City, Taiwan) Phase 1: Single-dose maximum tolerated dose (MTD): F18.7 was administered PO to groups of

2 male and 2 female (23 ± 3 g) ICR mice. Animals received an initial dose of 30 mg/kg. If the animals had no significant adverse effects within 60 min after treatment, the dose for the next cohort was increased. If one or more animals died or had significant adverse effects within 60 min after treatment, the dose for the next cohort was decreased. The testing stopped when all animals survived at the upper bound (200 mg/kg), or lower bound (3 mg/kg) had been reached. Full clinical examinations and body weight change were assessed. At each dose level, animals were observed, and mortality was noted daily after compound administration for three days. Animals were observed for the presence of acute toxic symptoms (mortality, convulsions, tremors, muscle relaxation, and sedation) and autonomic effects (diarrhea, salivation, lacrimation, vasodilation, piloerection, etc.) during the first 60 min and again at 120 min after administration. Body weights were recorded pre-dose and at 72 hours.

The next dose level was determined by the following scheme:

30 mg/kg, if no death, 100 mg/kg, if no death, 200 mg/kg (upper bound)

30 mg/kg, if no death, 100 mg/kg, if death, 50 mg/kg

30 mg/kg, if death, 10 mg/kg, if death, 3 mg/kg (lower bound)

30 mg/kg, if death, 10 mg/kg, if no death, 17 mg/kg

Phase 2: F18.7 was administered PO at 200 mg/kg, bid x5, 1h interval, 200 mg/kg, qd x5, and 150 mg/kg, bid x5, 8-hour interval to groups of 3 female CB.17 SCID mice (7 ± 1 week-old) for assessment of possible adverse effects. Animals were observed for the presence of acute toxic symptoms (mortality, convulsions, tremors, muscle relaxation, sedation) and autonomic effects (diarrhea, salivation, lacrimation, vasodilation, piloerection) during the first 50 (after 1st daily dose) or 60 (2nd daily dose) min after each dose. Body weights were recorded once daily for 8 days. The animals were observed for mortality twice daily for 8 days. In addition, plasma samples were collected at 0.5, 1, 2 and 5.3 hour(s) after the second dose on Day 4 (150 mg/kg, PO; bid x5 group) and at 0.5, 1, 2 and 6 hour(s) after the final dose on Day 5 (200 mg/kg, PO; qd x5 group). The exposure levels (ng/mL) of F18.7 in plasma samples were then determined by LC-MS/MS. *AUC_{last}* was calculated from the area under the plasma concentration-time curve from time zero to time of last measurable concentration.

In vivo PK studies with F18.7:

In vivo PK studies were performed by Pharmacology Discovery Services Taiwan (New Taipei City, Taiwan). F18.7 (30, 100, and 200 mg/kg, PO) was further administered to groups of 2 male and 2 female (23 ± 3 g) satellite ICR mice in PK study; the plasma and liver samples were harvested at 0.5 hour after administration. In addition, one additional group was dosed at 30 mg/kg and the plasma samples were harvested at 1 and 2 hour(s) after the treatment. The body and liver weights were recorded. The exposure

levels (ng/ml or ng/g) of F18.7 in plasma and liver samples were then determined by Liquid Chromatograph Tandem Mass Spectrometer (LC-MS/MS), and the plasma: liver ratios were calculated.

-

Anti-tumor activity in mouse models:

In vivo mouse models were generated and experiment with SK-OV-3 and AGS models performed by EPO, experimental pharmacology & oncology Berlin-Buch GMBH (Berlin, Germany). AGS model: AGS cells were cultured in F12-K medium (10%FCS, 1%PS) until P11. Freshly isolated cells (1×10^6) were subcutaneously transplanted to left flank of 8-week-old female mice in PBS/Matrigel (1:1). After achieving aTV group mean of 0.139 and 0.140cm³ mice were randomly assigned to three study groups with n=6 animals (TV: min. 0.106 / max. 0.229cm³) and were daily treated with either the vehicle (1% DMSO/ 10% solutol/ PBS), F18.7 (200 mg/kg in 1% DMSO / 10% solutol / PBS) or BGJ398 (10 mg/kg, in 2:1 PEG300/D5W). Tumor diameters were determined by calliper measurements 2x weekly, body weight (BW) was measured as parameter for tolerability 2x weekly.

SKOV3 model: SKOV-3 cells were cultured in McCoy's 5A (26600-023, ThermoFisher) media (10%FCS) until P7. Freshly isolated cells (1×10^6) with a viability of 98% were subcutaneously transplanted to left flank of 8-week-old female mice in PBS/Matrigel (1:1). After achieving aTV group mean of 0.138 and 0.143cm³ mice were randomly assigned to three study groups with n=8 animals (TV: min. 0.102 / max. 0.216cm³) after 48 h post cell transplantation and were daily treated either the vehicle (1% DMSO/ 10% solutol/ PBS), F18.7 (200 mg/kg in 1% DMSO / 10% solutol / PBS) or BGJ398 (10 mg/kg, in 2:1 PEG300/D5W). Tumor diameters were determined by calliper measurements 2x weekly, body weight (BW) was measured as parameter for tolerability 2x weekly.

-

Immunohistochemistry (IHC):

IHC of tumor sections was performed by Sophistolab (MuttENZ, Switzerland) on a Leica BondMax instrument using Refine HRP-Kits (Leica DS9800). All buffer-solutions were purchased from Leica Microsystems Newcastle, Ltd and used according to the manufacturer's guidelines. Paraffin-slides were de-waxed, pre-treated and incubated as follows: ER-solution 2 for 10 min at 95°C, ER-solution 2 for 20 min at 100°C and ER-solution 2 for 30 min at 100°C. pFRS2 ; Rabbit anti-Phospho FRS2 (PhosphoY 436, Abcam Limited; ab193363), dilution 1:150; phospho-p44/42 MAPK (Erk1/2) (Thr202/Tyr204) (D13.14.4E) Rabbit mAb (Cell Signaling Technology #4370), dilution 1:1600. The IHC images were captured digitally using a Nikon Epifluorescence Eclipse Ti2 equipped with a Nikon DS-Ri2 color and a Nikon DS-Qi2 monochrome camera.

Declarations

Acknowledgements:

This manuscript received funding from the Swiss Cancer league (SCL_KLS-3834-02-2016), the Swiss Cancer Research foundation (KFS-4853-08-2019), the Swiss National Science foundation (SNF_310030_188793) and the Stiftung Kinderkrebsforschung Schweiz. Mass-spectrometry was performed at the Functional Genomic Center Zürich.

Financial support: Martin Baumgartner: Swiss Cancer league (SCL_KLS-3834-02-2016), the Swiss Cancer Research foundation (KFS-4853-08-2019), the Swiss National Science foundation (SNF_310030_188793), Michael Grotzer: Stiftung Kinderkrebsforschung Schweiz (grant number: N/A).

Conflict of interest: *In vivo* studies were performed and financed under research collaboration agreement with Invasight AG.

References

1. Schneider, G. & Böhm, H. J. Virtual screening and fast automated docking methods. *Drug Discov. Today* **7**, 64–70 (2002).
2. Schneider, G. Virtual screening: An endless staircase? *Nat. Rev. Drug Discov.* **9**, 273–276 (2010).
3. Lu, H. *et al.* Recent advances in the development of protein–protein interactions modulators: mechanisms and clinical trials. *Signal Transduct. Target. Ther.* **5**, (2020).
4. Santhana Kumar, K. *et al.* TGF- β Determines the Pro-migratory Potential of bFGF Signaling in Medulloblastoma. *Cell Rep.* **23**, 3798–3812.e8 (2018).
5. Cavalli, F. M. G. *et al.* Intertumoral Heterogeneity within Medulloblastoma Subgroups. *Cancer Cell* **31**, 737–754.e6 (2017).
6. Xu, H., Lee, K. W. & Goldfarb, M. Novel recognition motif on fibroblast growth factor receptor mediates direct association and activation of SNT adapter proteins. *J. Biol. Chem.* **273**, 17987–17990 (1998).
7. Kouhara, H. *et al.* A lipid-anchored Grb2-binding protein that links FGF-receptor activation to the Ras/MAPK signaling pathway. *Cell* **89**, 693–702 (1997).
8. Dhalluin, C. *et al.* Structural basis of SNT PTB domain interactions with distinct neurotrophic receptors. *Mol. Cell* **6**, 921–929 (2000).
9. Helsten, T. *et al.* The FGFR Landscape in Cancer: Analysis of 4, 853 Tumors by Next-Generation Sequencing. 259–268 (2016)
10. Weiss, J. *et al.* Frequent and focal FGFR1 amplification associates with therapeutically tractable FGFR1 dependency in squamous cell lung cancer. *Sci. Transl. Med.* **4**, (2012).
11. Andre, F. *et al.* Human Cancer Biology Molecular Characterization of Breast Cancer with High-Resolution Oligonucleotide Comparative Genomic Hybridization Array. **15**, 441–452 (2009).

12. Di Stefano, A. L. *et al.* Actionable targets involving FGF receptors in gliomas: Molecular specificities, spatial distribution, clinical outcome and radiological phenotype. *J. Clin. Oncol.* **36**, 2005 (2018).
13. Konecny, G. E. *et al.* Second-line dovitinib (TKI258) in patients with FGFR2-mutated or FGFR2-non-mutated advanced or metastatic endometrial cancer: A non-randomised, open-label, two-group, two-stage, phase 2 study. *Lancet Oncol.* **16**, 686–694 (2015).
14. Verlingue, L. *et al.* Precision medicine for patients with advanced biliary tract cancers: An effective strategy within the prospective MOSCATO-01 trial. *Eur. J. Cancer* **87**, 122–130 (2017).
15. Loriot, Y. *et al.* Erdafitinib (ERDA; JNJ-42756493), a pan-fibroblast growth factor receptor (FGFR) inhibitor, in patients (pts) with metastatic or unresectable urothelial carcinoma (mUC) and FGFR alterations (FGFRa): Phase 2 continuous versus intermittent dosing. *J. Clin. Oncol.* **36**, 411 (2018).
16. Singh, D. *et al.* Transforming fusions of FGFR and TACC genes in human glioblastoma. *Science* (80-). **337**, 1231–1235 (2012).
17. Di Stefano, A. L. *et al.* Detection, characterization, and inhibition of FGFR-TACC fusions in IDH wild-type glioma. *Clin. Cancer Res.* **21**, 3307–3317 (2015).
18. Robertson, A. G. *et al.* Comprehensive Molecular Characterization of Muscle-Invasive Bladder Cancer. *Cell* **171**, 540–556.e25 (2017).
19. Turner, N. & Grose, R. Fibroblast growth factor signalling: from development to cancer. 1–14 (2010)
20. Gotoh, N. Regulation of growth factor signaling by FRS2 family docking/scaffold adaptor proteins. *Cancer Sci.* **99**, 1319–1325 (2008).
21. Zhang, K. *et al.* Amplification of FRS2 and Activation of FGFR/FRS2 Signaling Pathway in High-Grade Liposarcoma. *Cancer Res.* **73**, 1298–1307 (2013).
22. Li, J.-L. & Luo, P. MiR-140-5p and miR-92a-3p suppress the cell proliferation, migration and invasion and promoted apoptosis in Wilms' tumor by targeting FRS2. *Eur. Rev. Med. Pharmacol. Sci.* **24**, 97–108 (2020).
23. Wu, S. *et al.* Whole-genome sequencing identifies ADGRG6 enhancer mutations and FRS2 duplications as angiogenesis-related drivers in bladder cancer. *Nat. Commun.* 1–12 (2019)
24. *et al.* Hyperactivated FRS2 α -mediated signaling in prostate cancer cells promotes tumor angiogenesis and predicts poor clinical outcome of patients. **35**, 1750–1759 (2015).
25. Chew, N. J. *et al.* FGFR3 signaling and function in triple negative breast cancer. *Cell Commun. Signal.* **18**, 1–17 (2020).
26. Li, Q. *et al.* Pharmacologically targeting the myristoylation of the scaffold protein FRS2 α inhibits FGF/FGFR-mediated oncogenic signaling and tumor progression. *J. Biol. Chem.* **293**, 6434–6448 (2018).
27. Facchinetti, F. *et al.* Facts and New Hopes on Selective FGFR Inhibitors in Solid Tumors. **26**, 764–774 (2020).
28. Yamaoka, T., Kusumoto, S., Ando, K. & Ohba, M. Receptor Tyrosine Kinase-Targeted Cancer Therapy. *Int. J. Mol. Sci.* **19**, 1–35 (2018).

29. Chell, V. *et al.* Tumour cell responses to new fibroblast growth factor receptor tyrosine kinase inhibitors and identification of a gatekeeper mutation in FGFR3 as a mechanism of acquired resistance. *Oncogene* **32**, 3059–3070 (2013).
30. Li, Y. *et al.* FGFR-inhibitor-mediated dismissal of SWI/SNF complexes from YAP-dependent enhancers induces adaptive therapeutic resistance. *Nat. Cell Biol.* **23**, (2021).
31. Wolber, G. & Langer, T. LigandScout: 3-D pharmacophores derived from protein-bound ligands and their use as virtual screening filters. *J. Chem. Inf. Model.* **45**, 160–169 (2005).
32. Kumar, K. S. *et al.* Computer-assisted quantification of motile and invasive capabilities of cancer cells. *Sci. Rep.* **5**, 15338 (2015).
33. Guagnano, V. *et al.* Discovery of 3-(2,6-Dichloro-3,5-dimethoxy-phenyl)-1-{6-[4-(4-ethyl-piperazin-1-yl)-phenylamino]-pyrimidin-4-yl}-1-methyl-urea (NVP-BGJ398), A Potent and Selective Inhibitor of the Fibroblast Growth Factor Receptor Family of Receptor Tyrosine Kinase. *J. Med. Chem.* **54**, 7066–7083 (2011).
34. Hajduk, P. J., Meadows, R. P. & Fesik, S. W. NMR-based screening in drug discovery. *Q. Rev. Biophys.* **32**, 211–240 (1999).
35. Williams, S. V., Hurst, C. D. & Knowles, M. A. Oncogenic FGFR3 gene fusions in bladder cancer. *Hum. Mol. Genet.* **22**, 795–803 (2013).
36. Molina, D. M., Jafari, R., Ignatushchenko, M. & Seki, T. Monitoring Drug Target Engagement in Cells and Tissues Using the Cellular Thermal Shift Assay. *Science (80-.)*. **341**, 84–88 (2013).
37. Sridharan, S., Günthner, I., Becher, I., Savitski, M. & Bantscheff, M. Target Discovery Using Thermal Proteome Profiling. *Mass Spectrom. Chem. Proteomics* 267–291 (2019).
38. Savitski, M. M. *et al.* Tracking cancer drugs in living cells by thermal profiling of the proteome. *Science (80-.)*. **346**, (2014).
39. Jarzab, A. *et al.* Meltome atlas—thermal proteome stability across the tree of life. *Nat. Methods* **17**, 495–503 (2020).
40. Kumar, A., Voet, A. & Zhang, K. Y. J. Fragment based drug design: from experimental to computational approaches. *Curr Med Chem* **19**, 5128–5147 (2012).
41. Bale, T. A. FGFR- gene family alterations in low-grade neuroepithelial tumors. *Acta Neuropathol. Commun.* **6**, 1–9 (2020).
42. Liu, J. *et al.* Hyperactivated FRS2 α -mediated signaling in prostate cancer cells promotes tumor angiogenesis and predicts poor clinical outcome of patients. *Oncogene* **35**, 1750–1759 (2016).
43. Chikamori, M., Fujimoto, J., Tokai-Nishizumi, N. & Yamamoto, T. Identification of multiple SNT-binding sites on NPM-ALK oncoprotein and their involvement in cell transformation. *Oncogene* **26**, 2950–2954 (2007).
44. Bi, R. *et al.* ALK rearrangement: A high-frequency alteration in ovarian metastasis from lung adenocarcinoma. *Diagn. Pathol.* **14**, 1–10 (2019).

45. Matsumoto, T. *et al.* Anaplastic Lymphoma Kinase Overexpression Is Associated with Aggressive Phenotypic Characteristics of Ovarian High-Grade Serous Carcinoma. *Am. J. Pathol.* **191**, 1837–1850 (2021).
46. Manchado, E. *et al.* A combinatorial strategy for treating KRAS-mutant lung cancer. *Nature* **534**, 647–651 (2016).
47. Bernat-Peguera, A. *et al.* FGFR Inhibition Overcomes Resistance to EGFR-targeted Therapy in Epithelial-like Cutaneous Carcinoma. *Clin Cancer Res* **27**, 1491–1504 (2021).
48. Clement, M. S., Gammelgaard, K. R., Nielsen, A. L. & Sorensen, B. S. Epithelial-to-mesenchymal transition is a resistance mechanism to sequential MET-TKI treatment of MET-amplified EGFR-TKI resistant non-small cell lung cancer cells. *Transl. Lung Cancer Res.* **9**, 1904–1914 (2020).
49. Sung, V. Y. C. *et al.* Co-dependency for MET and FGFR1 in basal triple-negative breast cancers. *npj Breast Cancer* **7**, 1–15 (2021).
50. Gradient, P. A. & Sensitivity, I. Pure absorption gradient enhanced heteronuclear single quantum correlation spectroscopy with improved sensitivity. **26**, 10663–10665 (1992).

Tables

Tables 1-4 are in the supplementary files section.

Figures

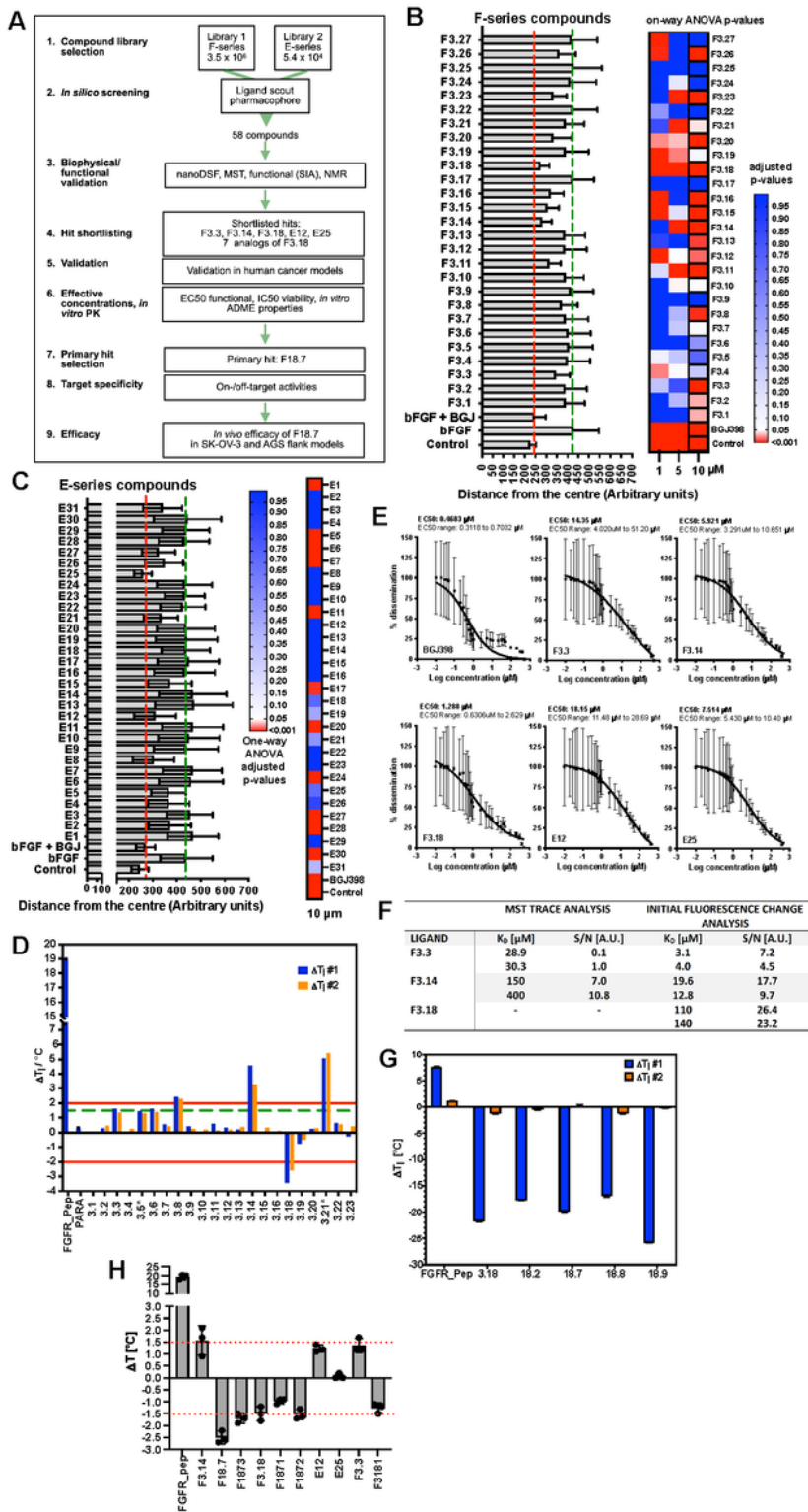


Figure 1

Compound identification A) Workflow of experimental procedures. **B)** Quantification of representative spheroid invasion assay (SIA) in DAOY cells treated with F3 series compounds at 10 μ M concentration. Mean and SD of distances of invasion and adjusted p-values from $n = 3$ technical replicas at 1, 5 and 10 μ M compound concentrations are shown. Red dotted line: Maximal repression of bFGF-induced invasion, green dotted line: Maximal bFGF-induced invasion. **C)** Quantification of representative SIA in DAOY cells

treated with E series compounds tested at 10 μ M concentration. Mean and SD of distances of invasion and adjusted p-values of n = 3 technical replicas are shown. Red dotted line: Maximal repression of bFGF-induced invasion, green dotted line: Maximal bFGF-induced invasion. **D)** nanoDSF analysis of a selection of F3 series compounds. Compound-induced DT_m of FRS2_PTB of two independent measurements are shown. * marks compounds with self-fluorescence exceeding the protein's fluorescence. **E)** EC_{50} of shortlisted compounds for collagen I invasion inhibition in DAOY cells. Log(Y) transformed and normalized invasion distances and corresponding SD of n = 3 technical replicas are plotted against compound concentrations. **F)** K_D of shortlisted F3 series compound binding to GB1-FRS2_PTB determined by measuring change in initial fluorescence using MST trace analysis. Fitting with a signal-noise ratio < 5 is considered no binding. **G)** nanoDSF analysis of GB1-FRS2_PTB binding of F3.18 analogs. Mean and SD of compound-induced DT_m at 10 μ M compound concentration is shown. n = 3 technical replicas. **H)** nanoDSF analysis of FRS2_PTB binding of F3.18 bioisosteres and shortlisted hits. Mean and SD of compound-induced DT_m at 10 μ M compound concentration is shown. n = 3 technical replicas.

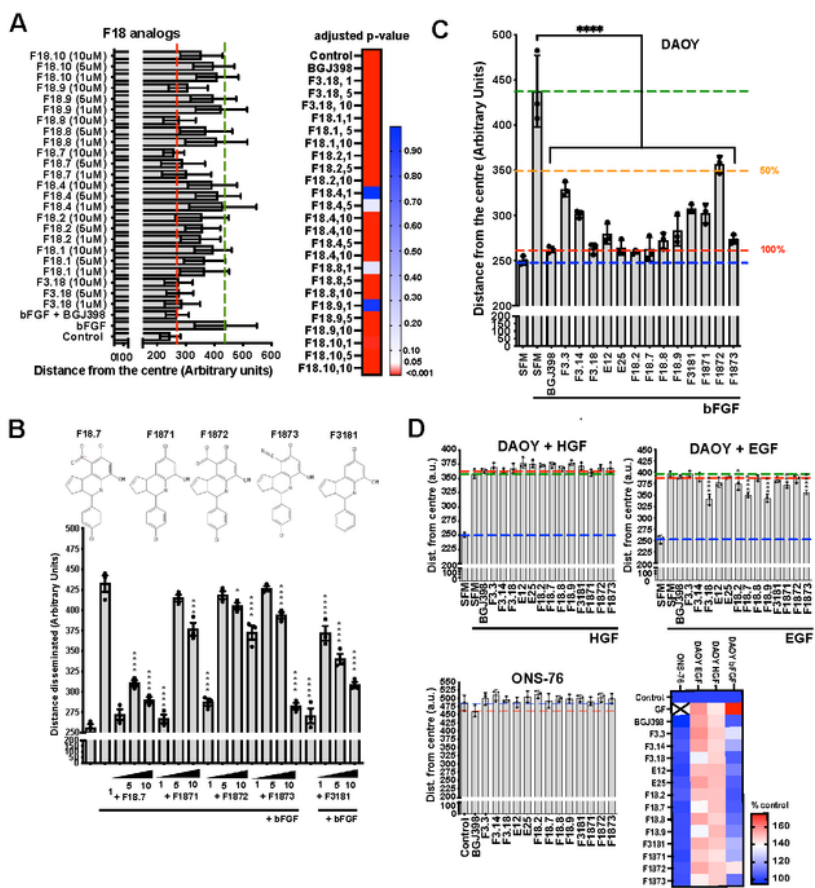


Figure 2

Identification of structural analogs and shortlisting of hits. **A)** Quantification of SIA in DAOY cells of structural F3.18 analogs. Mean and SD of distances of invasion and adjusted p-values from $n = 3$ technical replicas at $10 \mu\text{M}$ compound concentrations are shown. **B)** Quantification of SIA in DAOY cells with bioisosteres of F3.18 and F18.7 at 1, 5 and $10 \mu\text{M}$ compound concentrations. Mean and SEM of distances of invasion and adjusted p-values from $n = 3$ biological replicas at 1, 5 and $10 \mu\text{M}$ compound

concentrations are shown. **C)** Quantification of SIA analysis with bFGF-stimulated DAOY cells comparing anti-invasion efficacies of shortlisted compounds at 10 μ M concentration. Mean and SEM of distances of invasion and adjusted p-values from n = 3 biological replicas are shown. **D)** Upper tow panels: SIA analysis with HGF- or EGF-stimulated DAOY cells comparing anti-invasion efficacies of shortlisted compounds at 10 μ M concentration. Lower: SIA analysis with unstimulated ONS-76 cells comparing anti-invasion efficacies of shortlisted compounds at 10 μ M concentration. Heat map indicates relative change in invasion expressed as % of unstimulated control.

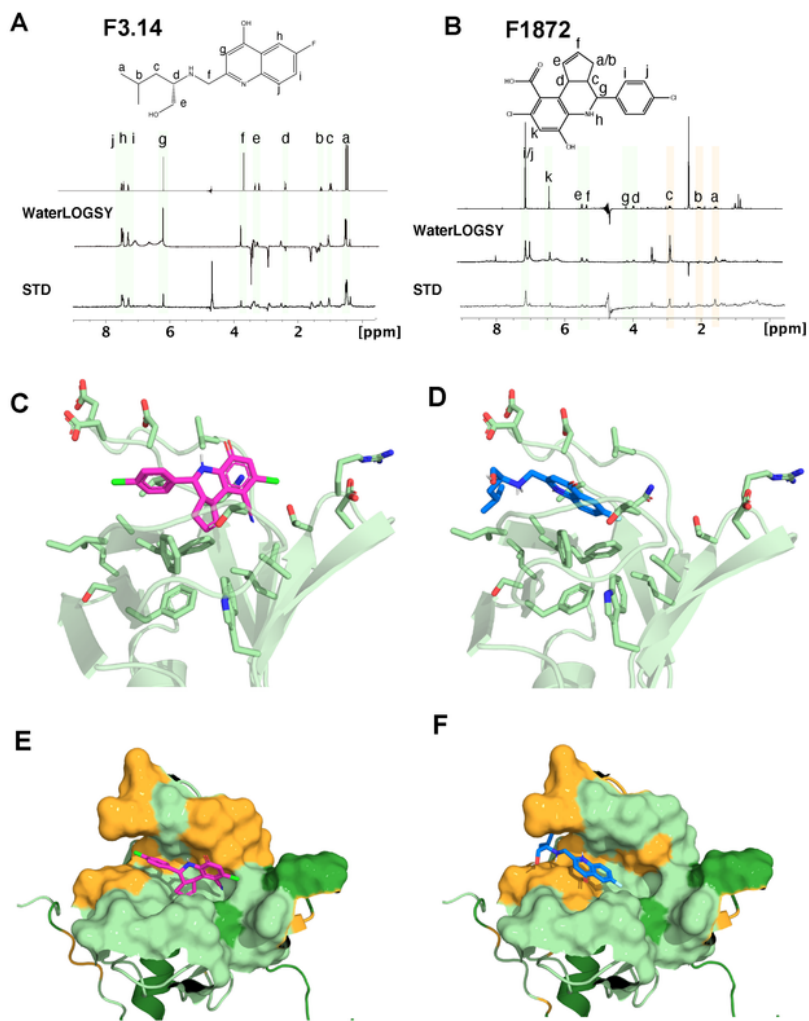


Figure 3

NMR screening of F3.14 and F1872. Reference spectrum with assignments of F3.14 **A)** and F1872 **B)** (upper trace) and WaterLOGSY (middle) and STD (bottom) of 25 μ M GB1-FRS2-PTB and 500 μ M F3.14 or F1872 at 280 K. Resonances exhibiting protein-interaction in the STD and/or the WaterLOGSY spectra are highlighted in light green, while resonances that might be obscured by buffer signals are indicated by light orange strips. **C,D** Cartoon of secondary structure showing the backbone trace of FRS2_PTB with

side-chains of the binding pocket depicted as sticks. Compounds F1873 (C,E) and F3.14 (D,F) are depicted as violet and blue sticks. D,F Protein surface within a 8 Å sphere around the ligand atoms. Residues with significant CSPs are highlighted in orange. Unassigned residues are shown in dark green.

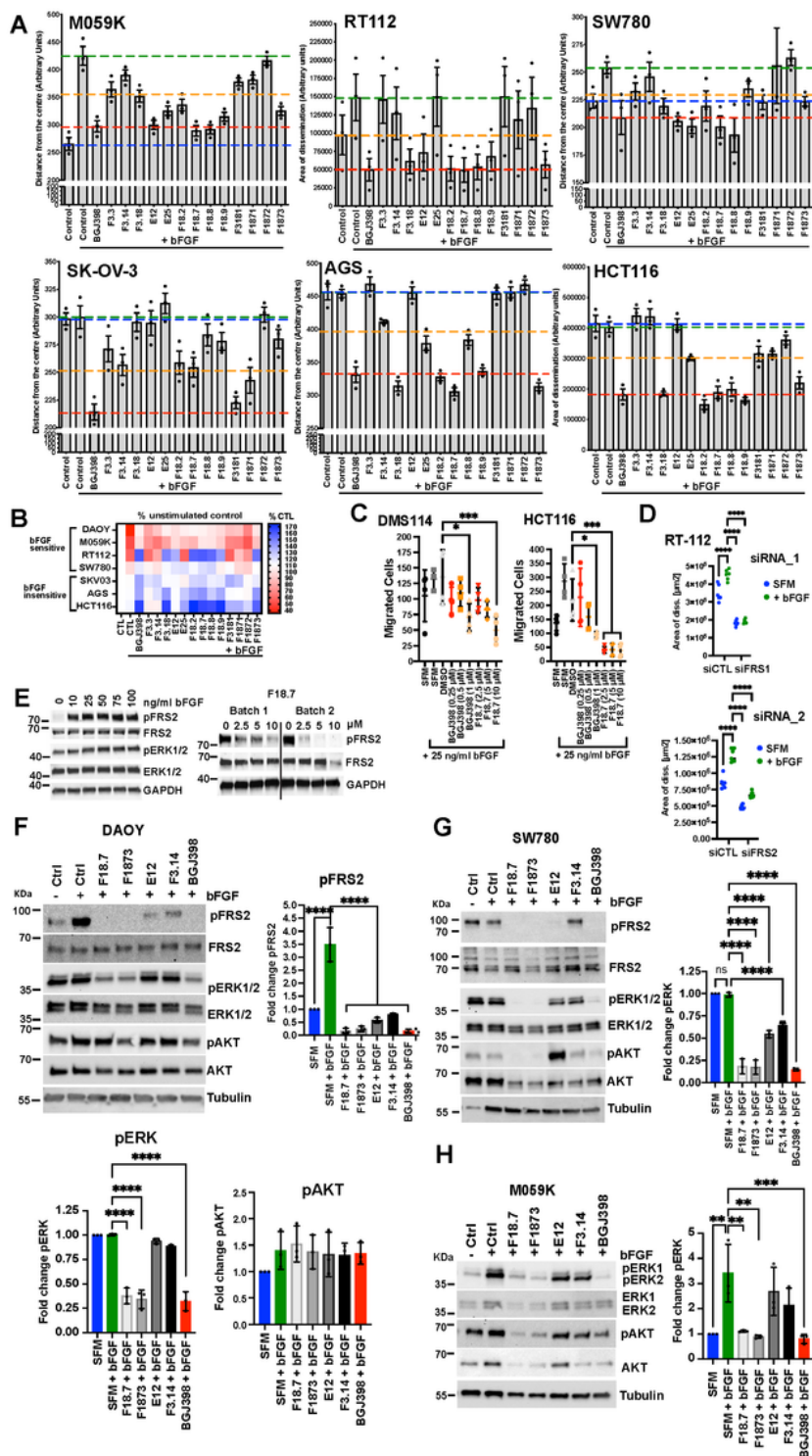


Figure 4

Shortlisted compounds variably block collagen I invasion and MAPK pathway activation in human cancer cell models. **A)** SIA analysis with shortlisted compounds in different human cancer cell models. Mean distance or area (RT-112) of invasion and SEM of $n = 3$ experiments at 10 μM compound concentrations are shown. Dotted lines: Blue: Basal mean invasion unstimulated, green: maximal mean invasion bFGF-stimulated, red: Maximal inhibition of invasion by BGJ398, orange: 50% of maximal mean invasion. **B)** Heat map of percent change of invasion relative to unstimulated control of SIA shown in A. **C)** Boyden chamber transwell migration assay. Mean and SD of $n = 4$ technical replicas and one-way ANOVA adjusted p-values are shown. **D)** SIA of RT-112 cells transfected with either two different FRS2-specific or their corresponding control siRNAs. Mean area of invasion of ≥ 6 spheroids, SD and one-way ANOVA adjusted p-values are shown. **E)** IB analysis of bFGF-induced FRS2 phosphorylation in DAOY cells (left) and of effect of F18.7 on bFGF-induced FRS2 phosphorylation. Batch 1 was kept frozen as DMSO stock for several months, batch 2 is a freshly dissolved stock. **F)** IB analysis of FRS2, ERK, and AKT phosphorylation in compound-treated DAOY cells stimulated with bFGF. **G)** IB analysis of FRS2 and ERK phosphorylation in compound treated SW780 cells stimulated with bFGF. **H)** IB analysis of ERK and AKT phosphorylation in compound treated M059K cells stimulated with bFGF. Bar diagrams in F-H depict quantification of phosphorylation relative to unstimulated control. Mean fold change of phosphorylation of $n = 3$ independent experiments, SD and one-way ANOVA adjusted p-values of comparison to SFM+bFGF are shown.

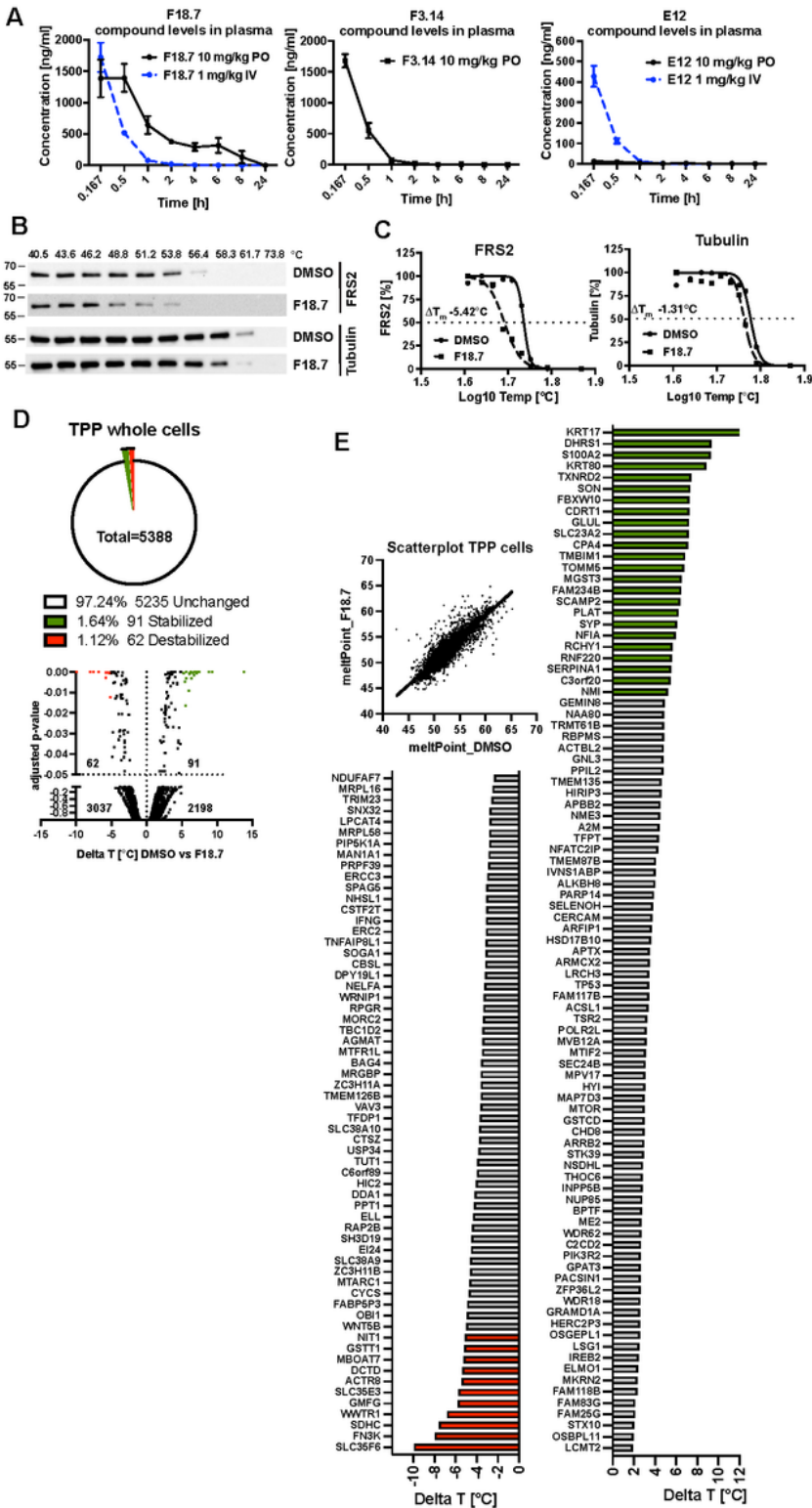


Figure 5

Bioavailability *in vivo* and on/off target activity of F18.7 in cells. A) Plasma exposure levels after 10 mg/kg peroral (PO, E12, F18.7) or 1 mg/kg intravenous (IV) (E12, F3.14 and F18.7) administration in mice quantified at intervals between 0.167 and 24 h. **B)** IB of FRS2 and tubulin in whole cell CETSA after DMSO or F18.7 treatment. **C)** Melting curves of FRS2 and tubulin from DMSO or F18.7-treated whole cell CETSA shown in B. **D)** Upper: Pie chart of percentage stabilized and destabilized proteins ($p < 0.05$) from

whole cell TPP from lysates analyzed in B. Lower: Volcano plot of ΔT_m from proteins of which high quality melting curves were obtained in both conditions. Red dots $\Delta T_m \geq -5^\circ\text{C}$, green dots: $\Delta T_m \geq 5^\circ\text{C}$. **E**) Scatterplot of all proteins with high quality melting curves in both conditions and bar plot with gene IDs of proteins with significantly altered T_m ($p < 0.05$). Red bars $\Delta T_m \geq -5^\circ\text{C}$, green bars: $\Delta T_m \geq 5^\circ\text{C}$.

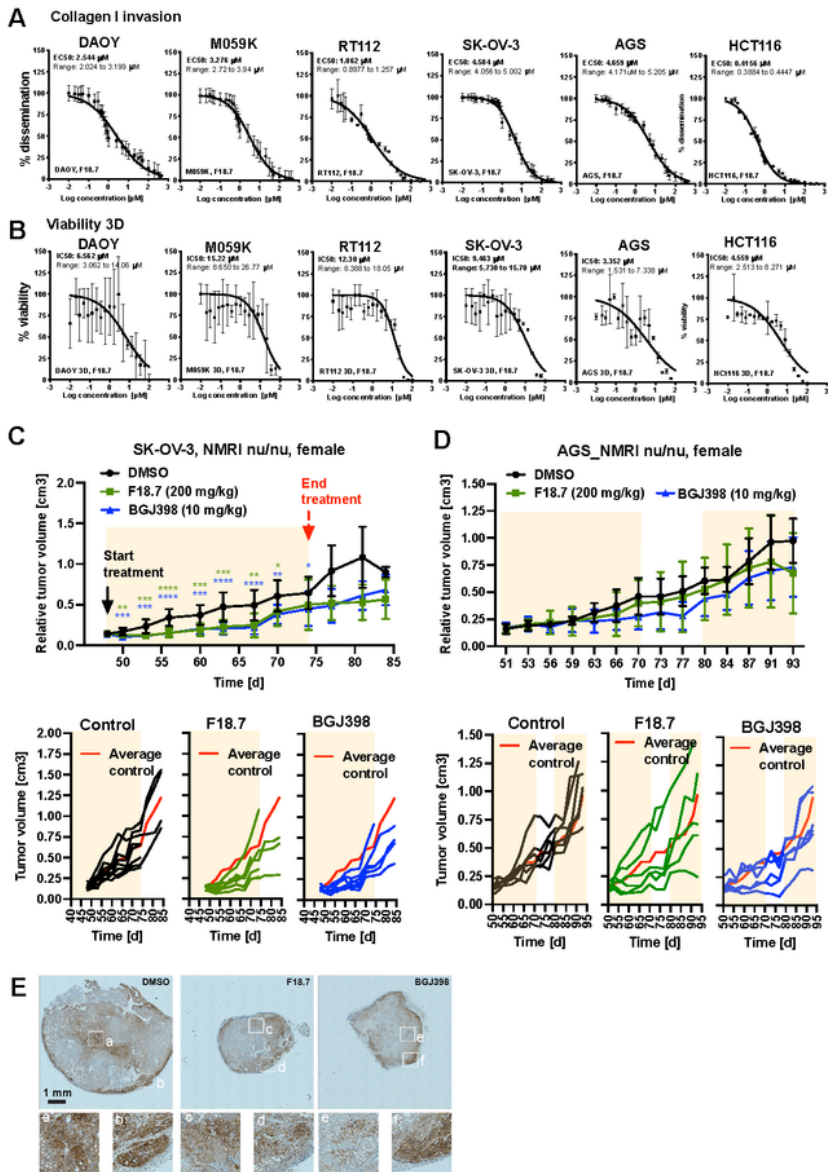


Figure 6

F18.7 reduces tumor growth *in vivo*. **A)** EC₅₀ curves of SIA with F18.7 in different human cancer cell models in the presence of 100 ng/ml bFGF. **B)** IC₅₀ curves of CellTiter Glo cell viability analysis with F18.7 in different human cancer cell models in full growth medium. **C)** Upper: Relative tumor volumes of SK-OV-3 flank tumor model of mice treated with DMSO, 10 mg/kg BGJ398 or 200 mg/kg F18.7. Lower: Tumor growth curves of individual tumors. **D)** Upper: Relative tumor volumes of AGS flank tumor model of mice treated with DMSO, 10 mg/kg BGJ398 or 200 mg/kg F18.7. Lower: Tumor growth curves of individual tumors. **E)** IHC analysis of pFRS2 staining in tumor samples of the SK-OV-3 flank tumor model at d75 (end of treatment).

Supplementary Files

This is a list of supplementary files associated with this preprint. Click to download.

- [Supplementaryfigures.pdf](#)
- [Tables.docx](#)
- [SupplementaryFile.docx](#)